EXPLORATION OF PHOTON ECHO IN A BOSE-EINSTEIN CONDENSATE

By

DAVID JUDSON GARY

Bachelor of Science in Physics

Old Dominion University

Norfolk, Virginia

2015

Submitted to the Faculty of the
Graduate College of the
Oklahoma State University
in partial fulfillment of
the requirements for
the Degree of
MASTER OF SCIENCE
July 2019

EXPLORATION OF PHOTON ECHO IN A

BOSE-EINSTEIN CONDENSATE

Thesis Approved by:

Dr. Gil Summy

_____

Thesis Adviser

Dr. Donna K. Bandy

_____

Dr. Emrah Turgut

_____

Name: DAVID JUDSON GARY

Date of Degree: JULY, 2019

Title of Study: EXPLORATION OF PHOTON ECHO IN A BOSE-EINSTEIN CONDENSATE

Major Field: PHYSICS

Abstract: A whole new area of experimental physics was opened up with the successful realization of the BEC in 1995. A BEC can be utilized to perform experiments where quantum phenomena can be seen on a macroscopic scale. In our experiment, we perform coherent manipulation of the hyperfine levels of Rb87 atoms in a BEC. We are, therefore, working with a macroscopic quantum two-level system. This allows us to test some of the fundamental concepts of atomic physics and laser spectroscopy. The aim of this experiment is to observe the recovery of inhomogeneous dephasing that each individual atom experiences in the form of a photon echo. This thesis will briefly review the process of creating a BEC and then transition into how one can utilize microwave spectroscopy and off-resonance lasers to manipulate a two-level system, all to realize a photon echo phenomena on a macroscopic scale. The setup of the lab will be discussed and how it was implemented in the experiment for data acquisition. Lastly, the results of the experiment will be put forward.

TABLE OF CONTENTS

Chapter Page

Chapter Page

LIST OF FIGURES

Figure Page

Figure Page

CHAPTER I

INTRODUCTION

Bose-Einstein Condensate (BEC) was first theorized by Albert Einstein in 1925. He used a statistical model put forth by Satyendra Nath Bose to derive the black body spectrum. In essence, he showed that if a group of atoms with integer spin (Bosons), is sufficiently cold, they can be thought of as a single quantum mechanical wave packet with a spacial profile characterized by the de-Broglie wavelength. This means that the de-Broglie wavelength represents the positional uncertainty in the momentum distribution and will increase with decreasing temperature. A BEC can be realized by lowering the temperature of bosonic atoms until the individual wave packets "overlap" creating a collection of indistinguishable particles. This "quantum soup" acts as a giant matter wave. Although a BEC is theoretically simple, it would take 70 years before it was experimentally realized.

A whole new area of experimental physics was opened up with the successful realization of the BEC in 1995. A BEC can be utilized to perform experiments where quantum phenomena can be seen on a macroscopic scale. In our experiment, we perform coherent manipulation of the hyperfine levels of Rb87 atoms in a BEC. We are, therefore, working with a macroscopic quantum two-level system. This allows us to test some of the fundamental concepts of atomic physics and laser spectroscopy [1].

The aim of this experiment is to observe the recovery of inhomogeneous dephasing that each individual atom experiences in the form of a photon echo. Photon echo falls under a category of echo processes the first of which, spin echo, was discovered in 1950 by E.L. Hahn

while studying nuclear resonance. Photon echo, the electric dipole analog, would be observed for the first time fourteen years later in 1964 by Kurnit, Abella, and Hartmann [2].

This thesis will briefly review the process of creating a BEC and then transition into how one can utilize microwave spectroscopy and off-resonance lasers to manipulate a two-level system, all to realize a photon echo phenomena on a macroscopic scale. The setup of the lab will be discussed and how it was implemented in the experiment for data acquisition. Lastly, the results of the experiment will be put forward.

CHAPTER II

LASER COOLING AND TRAPPING

For our purposes, two different cooling techniques are implemented in a two-step process to achieve a BEC. The first is the widely used Magneto-Optical Trap (MOT), and the second cooling technique is the Far Off Resonance Trap (FORT). The MOT is used to trap and cool atoms up to the recoil limit. The MOT has become a common trapping method used for this purpose in many labs, due to its effectiveness at catching room-temperature atoms, overall simplicity, and innate resilience to misalignment taking place over time and human-induced errors such as "alignment errors, laser frequency instabilities, magnetic field imperfections" [3], or any other form of uncertainty inevitably introduced by a human operator.

Once the MOT has prepared the atoms, The FORT utilizes evaporative cooling as well as trapping to reduce the phase space that the atoms occupy. This results in reduced temperatures and a denser sample of atoms, which ultimately results in a BEC. The following chapter will discuss both types of traps and why they are implemented

2.1 Magneto-Optical Trap

The MOT accomplishes two objectives, it confines the atoms to a central location and, in doing so, cools them. The cooling of the atoms is accomplished with a technique known as optical molasses. The setup up for optical molasses requires six lasers each propagating along either the ±x, ±y, or ±z direction. It is simplest if each laser is red detuned from the atomic

transition by the same amount. This is easily accomplished if the six beams to be generated are split from a larger source beam. When an atom, moving with velocity, v, encounters a pair of these beams, it will encounter a repulsive force because the redshifted laser photons opposing the motion of the atoms are blue-shifted into resonance with the atom, whereas redshifted laser photons moving with the atom are further redshifted away from resonance. It is clear that the cooling of the atoms is completely dependent on the velocity and not on their positions, and therefore, the cooling process occurs without confining the atoms. [3,4]

When the optical molasses setup is used in conjunction with an inhomogeneous magnetic quadrupole field, and the laser beams are made to be circularly polarized, another force is introduced. The requirement that the light is circularly polarized does not affect our previous discussion concerning the optical molasses, but it does enable a force that is dependent on the position of the atom in that magnetic field. A quadrupole field is produced with two coils, with radius, R, placed a distance, R, away from each other, Figure 2.1. The current in each coil is the same but travels in opposite directions from one another. The magnitude of the field produced by this setup is linear and shown in equation 2.1 [3].

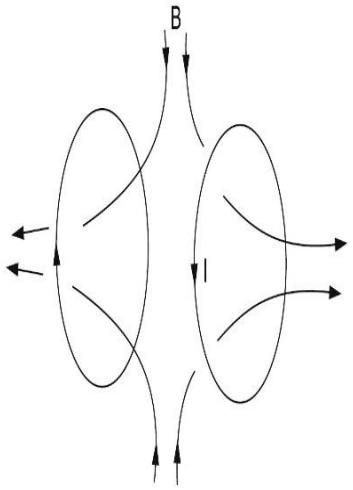

Figure 2.1: Anti-Helmholtz arrangement of the coils [4]

$$|B| = bz \tag{2.1}$$

where b is the magnetic field gradient and is dependent on the current and the size of the coils. A magnetic field with a $|B| > 0$ will split the Zeeman substate energy levels, making transitions that were the same in a $|B| = 0$ field slightly different. This is known as Zeeman shifts. The MOT setup takes advantage of Zeeman shifts in much the same way that optical molasses did the Doppler shifts. Arbitrarily choosing the positive polarization beam, σ_+, to be propagating in the

$+z$ direction and similarly σ_- in the $-z$, we see that atoms found on either side of the center, at $z = 0$, will encounter a restoring force. This is because atoms in the $-z$ interact with the σ_+ beam and atoms in the $+z$ interact with the σ_- beam, as shown in Figure 2.2.

Quantifying the dynamics of atoms in a MOT is a complicated endeavor. But if you make a few assumptions and limit your scope, a good understanding can be reached. To that end, our discussion will be valid only if the intensity of the lasers is kept low, allowing us to ignore stimulated emission effects. We will further limit our discussion to an area close to the center of the trap where the six beams intersect. Beginning with the absorption rates in steady-state for two counter-propagating beams, which take on Lorentzian profiles with half-width γ, the equation for the absorption profile is

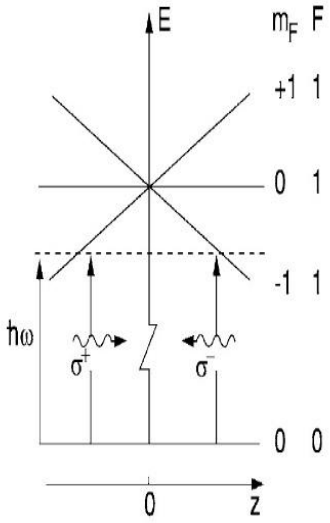

Figure 2.2: drawing representing how the polarized lasers interact with the Zeeman shifts [4]

$$R_-^+ = \frac{R_0}{\left[1 + \left(\frac{\delta \mp k v_z \pm \mu b z/\hbar}{\gamma'/2}\right)^2\right]} \qquad 2.2$$

where the detuning of the laser from resonance is $\delta = \omega_L - \omega_0$, the linewidth due to power broadening is $\gamma' = \gamma\sqrt{1 + s_0}$, the on-resonance absorption rate is $R_0 = \frac{\gamma}{2}\left(\frac{s_0}{1+s_0}\right)$ and the saturation parameter is $s_0 = \frac{I}{I_s}$. For convenience, the substitution $x = \frac{\mp kv \pm \mu b z/\hbar}{\gamma}$ is made and then an expansion around $x = 0$ only keeping the linear term is calculated, resulting in,

$$R_-^+ = \frac{-4 s_0 \delta}{\gamma\left[1 + s_0 + \left(\frac{2\delta}{\gamma}\right)^2\right]^2}\left(\mp k v_z \pm \frac{\mu b z}{\hbar}\right) \qquad 2.3$$

This expansion limits the discussion to slowly moving atoms near the center of the trap. The overall force on the atoms in the z direction is then given by [3,4]

$$F(v_z, z) = R_+\hbar\vec{k} + R_-\hbar\vec{k} \tag{2.4}$$

where the wave vectors, $\vec{k}$, are in opposite directions due to the counter propagating beams. With careful consideration of the signs, grouping terms, and solving for the acceleration, $\ddot{z} = \frac{F(v_z,z)}{M}$, you arrive at the familiar equation for damped harmonic motion, equation *2.5*, with coefficients β and α given in equation *2.6*

$$\ddot{z} + \frac{\beta}{m}\dot{z} + \frac{\alpha}{m}z = 0 \tag{2.5}$$

$$\beta = \frac{8s_0\delta k^2\hbar}{\gamma\left[1+s_0+\left(\frac{2\delta}{\gamma}\right)^2\right]^2} \qquad \alpha_z = \frac{8s_0\delta\mu bk}{\gamma\left[1+s_0+\left(\frac{2\delta}{\gamma}\right)^2\right]^2} \tag{2.6}$$

The atoms near the center of the MOT are subjected to a dampening constant β/m and have an oscillation frequency, $\sqrt{\alpha_z/m}$, about $z = 0$. Although this equation is only an examination of the behavior in the z direction, it is easy to see that the velocity term, $\dot{z}$, would be the same in either the x or y directions. The term dependent on the position requires a consideration of the symmetry of the anti-Helmholtz coil which produces the magnetic field mentioned in equation *2.1* but would also produce gradients in the x and y directions. The symmetry would imply that the gradients in the x and y directions are equal to each other. Furthermore, Maxwell's equation $\nabla \cdot B = 0$ absolutely holds,

$$\frac{\partial B_x}{\partial x} + \frac{\partial B_y}{\partial y} = -\frac{\partial B_z}{\partial z} \tag{2.7}$$

Because of this, you can see that the gradient, b value, in α is half as strong in the x or y directions and therefore equation *2.5* would require a small adjustment for the x or y directions, namely that

$$\alpha_z = \frac{1}{2}\alpha_x = \frac{1}{2}\alpha_y \tag{2.8}$$

In a typical MOT like our where the magnetic fields are modest and produce gradients of the order of ~10 G/cm equations *2.5* and *2.6* produce overdamped motion with a decay parameter $\beta' = \frac{\beta}{2m} - \sqrt{\left(\frac{\beta}{2m}\right)^2 - \frac{\alpha}{m}}$. The inverse of the decay parameter is the time it takes for the original distance from the center of the trap to be reduced to $1/e$ its initial value. Also of note is how the best dampening occurs when the term under the radical is equal to 0 resulting in

$$\beta = \frac{4m\mu}{\hbar k} b \tag{2.9}$$

So far, the discussion has been limited two forces that are introduced by the MOT setup, but a third force present caused by the interaction between the magnetic field and the magnetic moment of the atoms. This force is significantly smaller than the previously investigated forces and will not be discussed further. [3–5]

Despite the effectiveness of the MOT, it alone is unable to reduce the temperature enough to achieve a BEC. Theoretically, temperatures in the range of several milli-Kelvin are achievable and are referred to by the Doppler temperature or Doppler limit. Experiments have shown that a lower limit is possible because the cooling force described above is a result of a photon being absorbed and then emitted, resulting in a small momentum transfer.

$$p = \hbar k \tag{2.10}$$

The resulting change in velocity can be used to calculate the recoil temperature by taking the atoms average kinetic energy and inputting it into equation *2.11* which results in equation *2.12*.

$$\frac{1}{2} k_b T_r = \langle \mathrm{E}_k \rangle \tag{2.11}$$

$$T_r = \frac{\hbar^2 k^2}{k_b m} \tag{2.12}$$

This temperature on the order of several micro-Kelvin and is the temperature limit of our MOT [3]. It is several magnitudes higher than what is required for a BEC and, therefore, an additional cooling method must be implemented.

2.2 Far Off Resonance Trap

The FORT accomplishes two objectives. It first confines the atoms in a potential well and then subsequently will manipulate the depth of the well in order to cool the atoms. The trapping technique implemented is exactly what the name would suggest, that the laser is detuned such that $\delta \gg \Omega$. For our purposes, an attractive potential is desired, and therefore, the laser is red detuned. The depth of the dipole potential trap can be written as

$$U \approx \frac{3\pi c^2 \Gamma}{2\omega_0^3 \delta} I \tag{2.13}$$

where I is the intensity of the laser. Equation *2.13* can be compared to the scattering rate which is written as

$$\gamma_s \approx \frac{3\pi c^2}{2\hbar\omega_0^3} \frac{\Gamma^2 I}{\delta^2} \tag{2.14}$$

where Γ is the spontaneous scattering rate of the atom or the decay rate. With these two equations, you can easily arrive at a relationship between the decay rate and the dipole potential trap. When realized the comparison clearly illustrates that in the event of large detuning, the probability of a scattering event falls off faster than the size of the trap. Is also supports that an attractive potential is achieved when the detuning is negative [6–8].

The cooling process that is utilized here is evaporative cooling. The process entails lowering the depth of the trap, thereby allowing atoms with higher energy to escape. Although the process is technically a continuous one and should be described as such, a full description is beyond the scope of this thesis. Nevertheless, some insight into the process is required and, to

that end, a simple model that approximates the process as a single step will suffice in providing a qualitative understanding of the thermodynamics at work.

The simple model begins with an infinitely large trap, inside of which is a number of atoms, N, with a starting temperature, T. The depth of the trap is then lowered to a value $\eta K_B T$, where η is an arbitrary finite amount. Once the trap has been truncated, elastic collisions re-thermalize the sample of atoms, which allows for thermodynamic properties to be evaluated. Two parameters are of note, and from them, all other thermodynamic properties can be evaluated. The first is the ratio of atoms cooled to the total atoms before cooling began

$$\nu \approx \frac{\mathrm{N}'}{\mathrm{N}} \tag{2.15}$$

where the prime indicates final values. The second parameter is a measure of how much the temperature of the atoms remaining in the trap is reduced due to the atoms escaping the trap and is shown below

$$\gamma \approx \frac{\log(T'/T)}{\log \nu} \tag{2.16}$$

Knowing that our potential originates from a known Gaussian beam profile, we can, therefore, approximate our potential as harmonic. This assumption results in the other thermodynamic properties, volume and phase space density, related to γ and η, being represented as

$$V' = V\,\nu^{3\gamma/2}$$

$$\rho' = \rho\,\nu^{1-3\gamma} \tag{2.17}$$

The value ν can be calculated independently and used in conjunction with the starting number of atoms to determine the remaining number of atoms in the trap. This is done by with an integration of the product of the reduced density of states and the reduced energy of the trap.

The upper limit of the integration is the trap depth, $\eta K_B T$. For a harmonic trap, the value obtained is

$$\nu(\eta) = 1 - \frac{2 + 2\eta + \eta^2}{2e^{\eta}} \tag{2.18}$$

and the total energy of the atoms after truncation is

$$\alpha(\eta) = 3 - \frac{6 + 6\eta + 3\eta^2 + \eta^3}{2e^{\eta}} \tag{2.19}$$

The average total energy per atom in units of $K_B T$ is a ratio, $\alpha(\eta)/\nu(\eta)$. The overall effect of the evaporative cooling process is to lower the temperature and volume and in so doing, increase the phase space density. The BEC transition is realized when the phase space density exceeds 2.612 [3,6].

CHAPTER III

MICROWAVE SPECTROSCOPY

This section details how the microwaves interact with the $5^2 S_{1/2}$, F=1 and F=2 states or the hyperfine ground states of a Rb87 atom. These two states are several orders of magnitude removed from any higher F' states. It is therefore clear that the system is a quantum mechanical two-level system. If we approach the microwave radiation field from a classical perspective when discussing how the microwave radiation field interacts with the two-level system, the overall description of the coherent manipulation of the ground-state hyperfine levels becomes a semi-classical one, which is adequate. The discussion will begin with a time-dependent interaction represented by a Hamiltonian

$$\hat{H} = \hat{H}_a + \hat{V}(t) \tag{3.1}$$

which acts on a two-state system that can be characterized in the dressed state as

$$|\psi(t)\rangle = a(t)|+\rangle + b(t)|-\rangle \tag{3.2}$$

$$|+\rangle = \binom{1}{0};\ |-\rangle = \binom{0}{1} \tag{3.3}$$

The aim of this will be to develop concepts of the Optical Bloch Equations (OBEs), the Block Vector, and the Rabi Frequency, all operating under the Rotating Wave Approximation [9].

3.1 The Optical Bloch Equations

Typically when a microwave pulse is interacting with matter, electric and magnetic effects can be quantified, but due to the symmetry of the hyperfine S states in Rb87, the contributions of the electric dipole can be neglected, leaving only the interaction between the magnetic portion of the electromagnetic wave and the magnetic dipole moment of the Rb87 atom [7,10]. This interaction can be complicated to compute, but if limited to the $\Delta m = 0$ transitions, the treatment of the magnetic dipole is synonymous with an electric dipole [11]. Therefore the Hamiltonian for the magnetic dipole interaction takes the form

$$\hat{H} = \hat{H}_a - \sum_q \hat{\mu}_q \cdot \hat{B}(r_0) \tag{3.4}$$

where $\hat{H}_a$ is the unperturbed Hamiltonian and $\hat{B}(r_0)$ is the magnetic field operator at r_0. The $\sum_q \hat{\mu}_q$ is the total magnetic dipole moment operator and is shown in equation *3.5*, it accounts for contributions from the orbital, $\vec{L}$, and spin, $\vec{S}$, angular momenta of the valence electron and the angular momenta of the nucleus, $\vec{I}$ [7,10,12].

$$\sum_q \hat{\mu}_q = \hat{\mu}_1 + \hat{\mu}_2 + \hat{\mu}_3 = \hat{\mu}_L + \hat{\mu}_S + \hat{\mu}_I \tag{3.5}$$

Furthermore the operators $\hat{H}_a$ and $\hat{\mu}_q$ can be represented in terms of the Pauli spin matrices by calculating the matrix elements of $\hat{H}_a$ and $\hat{V}$ in the basis of the eigenstates that the system is in, leaving

$$\hat{H}_a = \frac{\hbar\omega_0}{2}\hat{\sigma}_3 \qquad \hat{\mu}_q = \vec{\mu}_{qr}\hat{\sigma}_1 - \vec{\mu}_{qi}\hat{\sigma}_2 \tag{3.6}$$

where ω_0 is the transition frequency between the $5^2 S_{1/2}$, F=1 and F=2 states. The quantities $\vec{\mu}_r$ and $\vec{\mu}_i$ are calculated by taking the positional expectation value in three dimensions, which traditionally amounts to a product of radial and angular integrals. However because we have limited ourselves to $\Delta m = 0$ transitions previously, the $\vec{\mu}_i$ portion in equation *3.6* can be

neglected due to symmetry. The radial integral will be discussed in the next section but for now, let's move on assuming that $\vec{\mu}_r$ is the sum of $\vec{\mu}_{Sr}$ and $\vec{\mu}_{Ir}$ which are themselves the results of such integrals [2,9].

An additional symmetry argument can be made that allows us to neglect contributions from the orbital angular momentum, i.e., $\vec{L} = 0$, because the interaction being considered is between two S states. Such argument results in our Hamiltonian taking the form [7,10]

$$\hat{H} = \frac{\hbar\omega_0}{2}\hat{\sigma}_3 - \left(\vec{\mu}_r \cdot \hat{B}\right)\hat{\sigma}_1 \qquad 3.7$$

Utilizing this Hamiltonian and working in the Heisenberg representation, it is a simple matter to calculate the rate of change of the Pauli matrices using the following equation.

$$i\hbar\dot{\hat{\sigma}}_n = \left[\hat{\sigma}_n, \hat{H}\right] \qquad \text{with} \quad n=1,2,3 \qquad 3.8$$

However, when doing so, it is convenient to ignore quantum correlations between the atom and the field, which focuses our interest in the expectation values of the Pauli matrices. Facilitating this is the notation in equation *3.9*. Another consequence of this convenient omission is that the electromagnetic wave in question can be treated as a classical wave. Also, the operator products that are present can be factored, and their expectation values calculated separately. Finally, if we also assume that the microwave radiation field induces a linearly polarized magnetic field, we arrive at equation *3.10* for the magnetic field

$$S_i(t) = \langle\psi(t)|\hat{\sigma}_n|\psi(t)\rangle \qquad 3.9$$

$$\langle\hat{B}(t,0)\rangle = \vec{B}(t,0) = B_0 cos(\omega t)\hat{z} \quad \text{with } r_0 = 0 \qquad 3.10$$

From all this, three equations can be obtained and are commonly referred to as the OBEs. The OBEs have many variations to them depending on the conditions considered, but these are suitable to begin our discussion

$$\dot{S}_1(t) = -\omega_0 S_2(t)$$

$$\dot{S}_2(t) = \omega_0 S_1(t) + \frac{2}{\hbar}\left(\vec{\mu}_r \cdot \langle \hat{B}(t) \rangle\right) S_3(t)$$

$$\dot{S}_3(t) = -\frac{2}{\hbar}\left(\vec{\mu}_r \cdot \langle \hat{B}(t) \rangle\right) S_2(t) \qquad 3.11$$

Equation *3.11* shows that the S vector traces out a path on the surface of the unit sphere. But a further simplification can make the path that is traced out much easier to interpret. Such a simplification begins by decomposing the interaction potential and defining the Rabi-Frequency [2,9].

3.2 The Rabi Frequency

Until the interaction potential is dealt with, solving the three equations in *3.11* cannot be done. Doing so will allow us to define the Rabi frequency, Ω, in the dressed state picture as

$$\langle + | \hat{V} | - \rangle = -\left(\vec{\mu}_r \cdot \langle \hat{B}(t) \rangle\right) = \frac{\hbar}{2}\Omega \qquad 3.12$$

If we remember that we are allowed to factor operator products and calculate the expectation values separately, we regain the interaction potential in question. Having already addressed the expectation value for the magnetic field in equation *3.10*, we need only find the result of $\vec{\mu}_r$ which was previously discussed [2,13]. To accomplish this, we note that the $\hat{\mu}_q$ operators can be represented in terms of the Bohr magneton, $\mu_B = e\hbar/2m_e$, and the respective Landé factor, g_q, as shown in the following equation *3.13*.

$$\hat{\mu}_q = \frac{\mu_B g_q \vec{q}}{\hbar} \qquad 3.13$$

We have already chosen to align ourselves along the atomic quantization axis, $\hat{z}$, when we defined the magnetic field in equation *3.10*. If we maintain that, we arrive at the following expression for the interaction potential.

$$\langle +|\hat{V}|-\rangle = -\frac{\mu_B\langle\hat{B}(t)\rangle}{\hbar}\langle +|(g_S S_z + g_I I_z)|-\rangle \tag{3.14}$$

To calculate this, we take advantage of the Clebsch-Gordon coefficients. The transition in question is between the F=1 and F=2 state, while continuing to maintain $\Delta m = 0$, and so we calculate equation *3.14* with those two states in mind

$$|1,1\rangle = \frac{\sqrt{3}}{2}\left|\frac{3}{2},\downarrow\right\rangle - \frac{1}{2}\left|\frac{1}{2},\uparrow\right\rangle$$

$$|2,1\rangle = \frac{1}{2}\left|\frac{3}{2},\downarrow\right\rangle + \frac{\sqrt{3}}{2}\left|\frac{1}{2},\uparrow\right\rangle$$

$$\langle 1,1|\hat{V}|2,1\rangle = -\frac{\mu_B\langle\hat{B}(t)\rangle}{\hbar}\langle 1,1|g_S S_z + g_I I_z|2,1\rangle$$

$$= \frac{\sqrt{3}\mu_B B_0 cos(\omega t)}{4}(g_S - g_I) \tag{3.15}$$

If we take note that $\langle 1,1|\hat{V}|2,1\rangle = \langle 1,-1|\hat{V}|2,-1\rangle$ we are left with one remaining $\Delta m = 0$ transition to calculate

$$|1,0\rangle = \frac{\sqrt{2}}{2}\left|\frac{1}{2},\downarrow\right\rangle - \frac{\sqrt{2}}{2}\left|-\frac{1}{2},\uparrow\right\rangle$$

$$|2,0\rangle = \frac{\sqrt{2}}{2}\left|\frac{1}{2},\downarrow\right\rangle + \frac{\sqrt{2}}{2}\left|-\frac{1}{2},\uparrow\right\rangle$$

$$\langle 1,0|\hat{V}|2,0\rangle = -\frac{\mu_B\langle\hat{B}(t)\rangle}{\hbar}\langle 1,0|g_S S_z + g_I I_z|2,0\rangle$$

$$= \frac{\mu_B B_0 cos(\omega t)}{2}(g_S - g_I) \tag{3.16}$$

We will now assert that our experiment maintains a constant amplitude in time on any given single microwave pulse, and we can then find the Rabi frequency that is representative of the interaction potential along the atomic quantization axis by combining equations *3.15* and *3.16* with *3.12* to arrive at

$$\Omega_0 = \frac{\mu_B B_0}{\hbar}(g_S - g_I)$$

$$\Omega_1 = \frac{\sqrt{3}\mu_B B_0}{2\hbar}(g_S - g_I) \qquad 3.17$$

which simplifies our previous rate equation *3.11*, allowing us to substitute in a scalar value, Ω, for the interaction potential. This substitution removes the last of the operators and vectors from the OBEs and places us in a position to make the Rotating Wave Approximation (RWA) [7,10].

3.3 The Rotating Wave Approximation and the Bloch Vector

Now that we have modified Equation *3.11* we can represent it as the vector S in a space with fixed unit vectors being acted upon by a known torque, τ_F.

$$\frac{d}{dt}S(t) = \tau_F \text{ x } S \qquad 3.18$$

When examining the torque expression, one component is found to oscillate back and forth rapidly. The resulting motion has no noticeable precession making that component completely ineffective. When we choose to neglect this component of the torque, the "approximation" in the RWA is realized, making the rate of change equations a little messy because trigonometric functions are introduced, but it is a simple matter to clean them up by placing S into a rotating frame such that

$$\begin{bmatrix} u \\ v \\ w \end{bmatrix} = \begin{bmatrix} cos(\omega t) & sin(\omega t) & 0 \\ -sin(\omega t) & cos(\omega t) & 0 \\ 0 & 0 & 1 \end{bmatrix} \begin{bmatrix} S_1 \\ S_2 \\ S_3 \end{bmatrix} \qquad 3.19$$

This rotation results in transforming equation *3.11* into three equations in a rotating frame

$$\dot{u} = -\delta v$$

$$\dot{v} = \delta u + \Omega w$$

$$\dot{w} = -\Omega v \qquad 3.20$$

Where $\delta = (\omega_0 - \omega)$ is the detuning from resonance. Knowing u, v and w are important, we will define the Bloch vector, $\rho = (u, v, w)$ and make this vector the next topic of consideration. The solutions to equation *3.20* are particularly simple when the detuning is equal to zero, i.e., the microwaves perturbing the system are on resonance. If that is the case, the solutions take the form of a rotation, which shows the Bloch vectors precession on the v, w plane. [2]

$$\begin{bmatrix} u \\ v \\ w \end{bmatrix} = \begin{bmatrix} 1 & 0 & 0 \\ 0 & cos(\Omega t) & sin(\Omega t) \\ 0 & -sin(\Omega t) & cos(\Omega t) \end{bmatrix} \begin{bmatrix} u_0 \\ v_0 \\ w_0 \end{bmatrix} \qquad 3.21$$

3.4 The Bloch Vector

Much like equation *3.11*, equation *3.20* traces out a path on the unit sphere, which confines the Bloch vector to the surface of the unit sphere. The state of the system can be determined at any given moment by locating the position of the Bloch vector on the unit sphere. To illustrate this, note that there are two spinor basis states that satisfy our system

$$|\psi^+(\theta, \varphi)\rangle = \cos\frac{\theta}{2}|+\rangle + e^{i\varphi}\sin\frac{\theta}{2}|-\rangle$$

$$|\psi^-(\theta, \varphi)\rangle = -e^{-i\varphi}\sin\frac{\theta}{2}|+\rangle + \cos\frac{\theta}{2}|-\rangle \qquad 3.22$$

Where $\theta = \Omega t$. If we calculate the expectation value of the Pauli spin vector, $\vec{\sigma} = (\sigma_1, \sigma_2, \sigma_3)$, using these spinor basis states we get the familiar coordinate vector in terms of the Euler angles [14]

$$\langle\psi^+|\vec{\sigma}|\psi^+\rangle = -\langle\psi^-|\vec{\sigma}|\psi^-\rangle = (\sin\theta\cos\varphi\,, \sin\theta\sin\varphi\,, \cos\theta) \qquad 3.23$$

Physical meaning can be found in the Bloch vector by understanding that the three axes u, v and w are the expectation values of the Pauli spin matrices in the rotating frame. Simply put, w represents the inversion, u and v are interpreted as components of the atoms magnetic dipole moment operator that are in-phase and in-quadrature with the magnetic field. We can further see that v is the absorptive component of the dipole moment because it is the component that is coupled with energy changes in the system, as seen in the third part of equation *3.20*. Knowing this makes u the dispersive component. This interpretation is further supported by equation *3.21* [2]

3.5 Microwave Rabi Pulses

In previous sections have seen how equation *3.20*, under the assumption of zero detuning, can be utilized to predict how the Bloch vector will precess about the Bloch sphere in time. Several methods are available to solve equation *3.20* while still accounting for the detuning, but an equivalent and easier method can be made using the two spinor basis states, defined in equation *3.22*, and acting on $|\psi(0)\rangle$, where $|\psi(0)\rangle$ is defined in equation *3.2*.

$$\langle\psi^+|\psi(0)\rangle = a_0 cos\frac{\theta}{2} + b_0 e^{-i\varphi} sin\frac{\theta}{2}$$

$$\langle\psi^-|\psi(0)\rangle = -a_0 e^{i\varphi} sin\frac{\theta}{2} + b_0 cos\frac{\theta}{2} \qquad 3.24$$

The results of equation *3.24* are often written in the form of a two-component spinor and when done so is representative of the state of our system after it has been exposed to a microwave pulse for a period of time, i.e., solutions for $a(t)$ and $b(t)$ [15]

$$\begin{pmatrix}\langle\psi^{+}|\psi(0)\rangle\\ \langle\psi^{-}|\psi(0)\rangle\end{pmatrix}=\begin{pmatrix}a(t)\\ b(t)\end{pmatrix}=\begin{pmatrix}a_0 cos\frac{\theta}{2}+b_0 e^{-i\varphi}sin\frac{\theta}{2}\\ -a_0 e^{i\varphi}sin\frac{\theta}{2}+b_0 cos\frac{\theta}{2}\end{pmatrix} \quad 3.25$$

One could easily see that this could be put into matrix form.

$$\begin{pmatrix}\cos\frac{\theta}{2} & e^{-i\varphi}\sin\frac{\theta}{2}\\ -e^{i\varphi}\sin\frac{\theta}{2} & \cos\frac{\theta}{2}\end{pmatrix}\begin{pmatrix}a_0\\ b_0\end{pmatrix}=\begin{pmatrix}a(t)\\ b(t)\end{pmatrix} \quad 3.26$$

In many experiments involving microwave spectroscopy π and $\pi/2$ pulses are particularly important (my experiment is no different). Therefore, let us examine the results of equation *3.25* for both pulses with the ground state being our initial state. While doing so, we introduce a notation change for equation *3.2*.

$$|\psi(t)\rangle = |\psi_{\theta,\varphi}\rangle$$

$$|\psi_{\frac{\pi}{2},\varphi}\rangle = \frac{\sqrt{2}}{2}|+\rangle - \frac{\sqrt{2}}{2}e^{i\varphi}|-\rangle$$

$$|\psi_{\pi,\varphi}\rangle = -e^{i\varphi}|-\rangle \quad 3.27$$

The modulus squared, of the coefficients $a(t)$ and $b(t)$ will provide the populations of each state, doing so results in the expected distributions.

CHAPTER IV

LASER PERTURBATIONS

In between the microwave pulses, we expose our BEC to a far-off resonance laser with the aim of perturbing the system through AC-Stark shifts which are dependant on the intensity of the laser. It is also common knowledge that the intensity of a laser a function of spot size in that point on the edge of the beam profile will have a lower intensity than the intensity in the middle of the beam. These two facts result in each atom experiencing a different AC-Stark shift, Which in turn results in a distribution of dephasing throughout the sample. The following sections outline how the energy levels are affected by the AC-Stark shift and how that enables the photon echo phenomenon.

4.1 AC-Stark Shift

When far-detuned laser light with intensity, I, interacts with the atomic level of an atom, the effects can be approximated with a high degree of accuracy using second-order perturbation theory. Where the perturbing Hamiltonian is $\hat{V} = -\hat{\mu}E$. The development is synonymous with the discussion in the previous chapter and when assuming a two-level system, can be shown to result in an energy shift of the form

$$E_s = \pm \frac{|\langle + |\hat{\mu}| - \rangle|^2}{\delta} |E|^2 \tag{4.1}$$

Knowing that the time-average intensity, $\langle I \rangle$, of the laser is related to the produced electromagnetic wave as

$$\langle I \rangle = 2\varepsilon_0 c|E_0|^2 \tag{4.2}$$

And that the dampening rate or decay rate, calculated using the oscillator model, is represented as

$$\Gamma = \frac{\omega_0^3}{3\pi\varepsilon_0\hbar c^3}|\langle +|\hat{\mu}|-\rangle|^2 \tag{4.3}$$

we are then able to express the energy shift in terms of these two quantities as

$$E_s = \pm\frac{3\pi c^2\Gamma}{2\omega_0^3\delta}I \tag{4.4}$$

This energy shift is known as the AC-Stark shift. Notice that it is equivalent to our quantity for the dipole potential trap in equation *2.13*. Meaning that the light-shifted ground state can act as a traping potential and is relevant when considering the motion of the atoms, but only if the intensity gradient is large enough, as is the case with the CO_2 laser during BEC formation. When considering the interaction of the shifting laser with the BEC, the spot size results in a much smaller gradient and, in turn, has a negligible overall traping effect. What is relevant, when considering the shifting laser, is that the AC-Stark Shift is dependant on the laser intensity and that a gradient, even a gentle one, will create an inhomogeneous distribution in the AC-Stark Shift [8].

4.2 Photon Echo

Although the development of the OBEs in previous sections did not take into consideration the phenomenological decay constants, such a development is possible. Keeping in mind the absence of any population decay time, the OBEs take on the form

$$\dot{u} = -\delta v - \frac{u}{T}$$

$$\dot{v} = \delta u + \Omega\, w - \frac{v}{T}$$

$$\dot{w} = -\Omega\, v \qquad 4.5$$

It is clear that these equations confine any dampening process due to T to the u-v plane, and therefore is not related to any energy-loss process. T can be represented as

$$\frac{1}{T} = \frac{1}{T'} + \frac{1}{T^*} \qquad 4.6$$

where T' is an irreversible dampening constant that is due to incoherent interactions that homogeneously affect all atoms. T^* is a reversible dampening constant, Its effect is to damp out the polarization density due to the dephasing of the individual dipole moments of the atom. There are various phenomena that can cause this effect but in our case, the dephasing can be attributed to each atoms exposure to a Gaussian laser profile resulting in varied AC-Stark shifts for each atom in the BEC sample. In our experiment, and all experiments where oscillator type phenomena are expected, T^* is the dominant dampening force. [2,9]

The photon echo phenomena aims to recover the dephasing caused by the dampening constant T^*. Accomplishing this experimentally requires a precise series of pulses. The process begins with exposure to a $\pi/2$ pulse which puts the system into a superposition of states. Then after waiting for a time τ, the aim is to modify the individual oscillating frequencies in a manner equivalent to a reversal by applying a π pulse with a phase of 180 degrees, this causes the partially dephased vectors to rotate about the u-axis, thereby constructing a macroscopic rephasing of the individual dipole moments at time 2τ. In our experiment, at time 2τ, we perform a phase scan of the atoms in intervals of 45 degrees and take note of the population distribution [2].

For a more quantitative development of the photon echo process, let us assume that during the $\pi/2$ and π pulses that no dephasing occurs and therefore any dephasing of the dipole moments is confined to the gaps in between pulses. We begin with the fact that the two-level system can be characterized as

$$|\psi(t)\rangle = e^{\frac{-iE_1 t}{\hbar}} \cos\frac{\Omega t}{2}|+\rangle + e^{\frac{-iE_2 t}{\hbar}} \sin\frac{\Omega t}{2}|-\rangle \tag{4.7}$$

which can be manipulated without loss of generality to arrive at

$$|\psi(t)\rangle = \cos\frac{\Omega t}{2}|+\rangle + e^{\frac{-i(E_2-E_1)t}{\hbar}} \sin\frac{\Omega t}{2}|-\rangle \tag{4.8}$$

A comparison with equation *3.22* shows us that

$$\varphi = \frac{-(E_2 - E_1)t}{\hbar} \tag{4.9}$$

When far-off resonant laser light is incident on a sample of atoms, the effect on the Bloch vector is a rotation about the w-axis. This is represented in equation 2.26 as the quantity φ. We also know from the discussion in the previous section the effect of the Stark shift on the energy levels of the atoms. Therefore after a time τ, our value for φ is

$$\varphi' = \frac{-(E_2 - E_1 + 2E_s)\tau}{\hbar} = \frac{-(E_2' - E_1')\tau}{\hbar} \tag{4.10}$$

After a $\pi/2$ pulse our system is the state $|\psi_{\frac{\pi}{2},\varphi}\rangle$, as was shown in equation *3.27*. Allowing the state to develop under the influence of the shifting laser for a time τ, we arrive at the state

$$\left|\psi_{\frac{\pi}{2}}(\varphi')\right\rangle = \frac{\sqrt{2}}{2}|+\rangle - \frac{\sqrt{2}}{2}e^{i\varphi'}|-\rangle \tag{4.11}$$

which we place into a more convenient form

$$\left|\psi_{\frac{\pi}{2}}(\tau)\right\rangle = \frac{\sqrt{2}}{2}\left(e^{\frac{-iE_1'\tau}{\hbar}}|+\rangle - e^{\frac{-iE_2'\tau}{\hbar}}|-\rangle\right) \tag{4.12}$$

We now wish to expose our sample to a π pulse and to do so it is convenient to reorder equation *3.22* as well

$$|\psi_\theta^+\rangle = e^{\frac{iE_2't'}{\hbar}}\cos\frac{\theta}{2}|+\rangle + e^{\frac{iE_1't'}{\hbar}}\sin\frac{\theta}{2}|-\rangle$$

$$|\psi_\theta^-\rangle = -e^{\frac{iE_2't'}{\hbar}}\sin\frac{\theta}{2}|+\rangle + e^{\frac{iE_1't'}{\hbar}}\cos\frac{\theta}{2}|-\rangle \qquad 4.13$$

With these more convenient forms in place, we calculate the state of our system after the π pulse to be

$$\begin{pmatrix}\langle\psi_\pi^+|\psi_{\frac{\pi}{2}}(\tau)\rangle\\ \langle\psi_\pi^-|\psi_{\frac{\pi}{2}}(\tau)\rangle\end{pmatrix} = -\frac{\sqrt{2}}{2}\begin{pmatrix}e^{-i\left(-\varphi'+\frac{E_1't}{\hbar}\right)}\\ e^{-i\left(\varphi'+\frac{E_2't}{\hbar}\right)}\end{pmatrix} \qquad 4.14$$

The state of this system can also be ordered to arrive at

$$|\psi(t)\rangle = -\frac{\sqrt{2}}{2}\left(e^{\frac{i\varphi'}{2}\left(\frac{t}{\tau}-2\right)}|+\rangle + e^{-\frac{i\varphi'}{2}\left(\frac{t}{\tau}-2\right)}|-\rangle\right) \qquad 4.15$$

Recall that $\hat{\mu}$ is a vector operator with odd parity, so that a calculation of the dipole moment for each atom results in

$$\langle\psi^*(t)|\hat{\mu}|\psi(t)\rangle = \langle+|\hat{\mu}|-\rangle e^{i\varphi'\left(\frac{t}{\tau}-2\right)} \qquad 4.16$$

As discussed previously there is an intensity gradient present in the spot size of the laser beam and it is that beam which provides the AC-Stark shifts. Furthermore, it is the AC-Stark shift which defines the difference between φ and φ' in equations *4.9* and *4.10*. Therefore it is clear that φ' is different for each atom, which, upon inspection of equation *4.16*, leads to the logical conclusion that the only time the dipole moments will be in sync is when $t = 2\tau$. This is exactly what any echo process would predict, a rephrasing at 2τ [4].

CHAPTER V

EXPERIMENTAL SETUP

There are many steps along the way to BEC creation, optical molasses, trapping atoms in the MOT, and then the FORT. The lab has two different laser tables with setups to accomplish these tasks. The first table houses the main laser and re-pump laser. The second table we have set up the shifting laser, vacuum chamber, and CO_2 laser. For safety reasons involving the CO_2 laser, the second table is easily cordoned off with thick black curtains. This also reduces the ambient light in the vacuum chamber. The following sections of this chapter will detail the setup of the two laser tables in our lab.

5.1 The Main Laser

The main laser system is a series of four lasers, designated as the master laser, master slave laser, slave 1, and slave 2. They are designated as such because, through optical techniques, the slave lasers adopt the same mode that as the master laser. The master laser is a TOPTICA, DL100 laser, and it has a grating to make very fine adjustments to the frequency. The entire laser is mounted to a temperature controlled base, and when powered on has an output of 20mW in the continuous wave (CW) mode. The grating on the master laser is used to find the frequency mode, for Rb87, corresponding to the transition between the $5^2 S_{1/2}$, F=2 ground state and at a point 133 MHz below the $5^2 P_{3/2}$, F'=3 excited state. This is verified by siphoning off a small portion of the Main laser's light and splitting it into two beams before passing both beams through a Rb87 cell and collecting one of the beam's light with a photodiode (either Thorlabs; DET-210, PDA-400, or homemade FDS010, FDS100 photodiodes were employed). Then it is a simple matter, by

using laser spectroscopy, to inspect the saturated absorption spectrum using an oscilloscope to ensure we are locked onto the correct mode.

As previously mentioned the output power of the main laser is 20mW in CW mode, unfortunately, to achieve our goals more power is required. Therefore three homemade diode lasers (master slave, slave 1, and slave 2) were utilized to augment the output power of the main laser in a cost-effective manner. A detailed schematic of the main laser was included in Figure 5.1 Each slave laser was a CW mode laser with approximately 100mW output power, mounted to a temperature controlled base. Each of the lasers was placed in a series, and by utilizing injection-locking techniques, we ensured that each of the slave lasers adopted the mode of master laser. This was verified in the same way as with the master laser by examining the saturated absorption spectrum on a scope. The entire process requires daily alignment to the mirrors involved and adjustments of each lasers current as well as precise control over the temperature of each laser diode. It is important to note that steps were taken to ensure that "self-following" did not occur by utilizing Faraday rotors and half-wave plates to prevent any light from being reflected back into the Main laser. Also of note, is that pairs of anamorphic prisms were used in order to ensure that the laser light took on a circular shape instead of an elliptical one. These processes are elaborated in [6], [7], and [16].

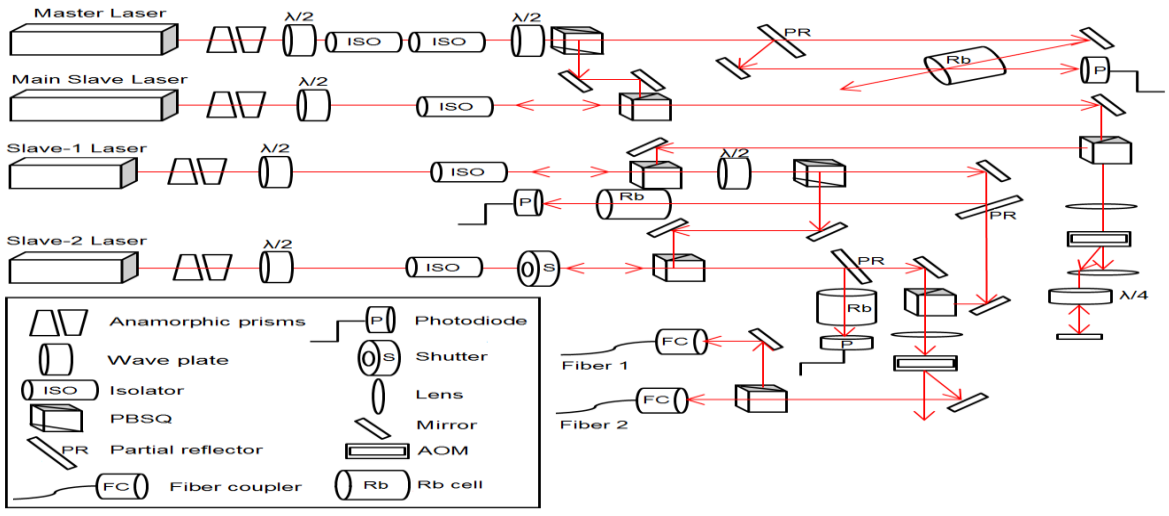

Figure 5.1: A schematic layout of the Main laser used for trapping, cooling, and imaging the atoms [7].

To achieve the BEC, the main laser must be detuned to three different frequencies. Two of those frequencies are required to provide the dampening force on the atoms. The first frequency will enable Doppler cooling through the process known as optical molasses. The other interacts with the Zeeman states to provide a force that is pointed radially inward and traps the atoms. Each one of these acts in tandem and is detailed in section 2.1. The third frequency detuning required is for imaging the atoms. In the middle of the series of lasers, after the master slave has adopted the mode of the main laser but before injection locking has occurred for the other two slave lasers, a detuning of the frequency is conducted by employing an Acousto-Optic Modulator (AOM) in a double pass configuration shown in Figure 5.2. For the double-pass configuration to work properly, steps must be taken to ensure that the beam propagates along the same path on both trips through the AOM. The specific process that was undertaken in our lab to accomplish this is detailed in [6,7,16]. Only positive first-order light is allowed to propagate when it passes through the AOM. This is accomplished on both passes through the AOM by blocking zeroth-order light on a wave plate.

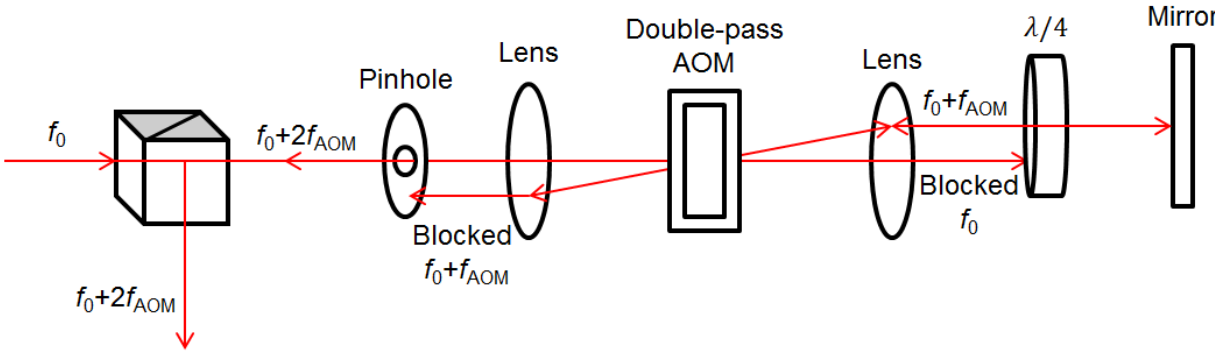

Figure 5.2: A schematic layout of the double pass configuration used in conjunction with the AOM [7].

An AOM creates a diffraction grating by vibrating a crystal with sound waves, and that allows us to control the magnitude and frequency of each order of light in the diffraction pattern. Although minor adjusting of the angle of incidence into the AOM is required periodically to fine-tune the detuning settings. The main operating procedure is to control the AOM via a

LabVIEW program and have the frequency the AOM vibrates alternate between three different settings to achieve the required detuning's from the $5^2 S_{1/2}$, F=2 ground state to the $5^2 P_{3/2}$, F'=3 excited state. The three detuning's, δ_i, which must interact with the atoms to form the BEC and image it properly are listed below and are illustrated in Figure 5.3.

1) -15MHz detuning to facilitate Zeeman splitting interactions for MOT creation

2) -80 MHz detuning to facilitate Doppler cooling in optical molasses

3) 0 MHz detuning or on resonance light to facilitate imaging

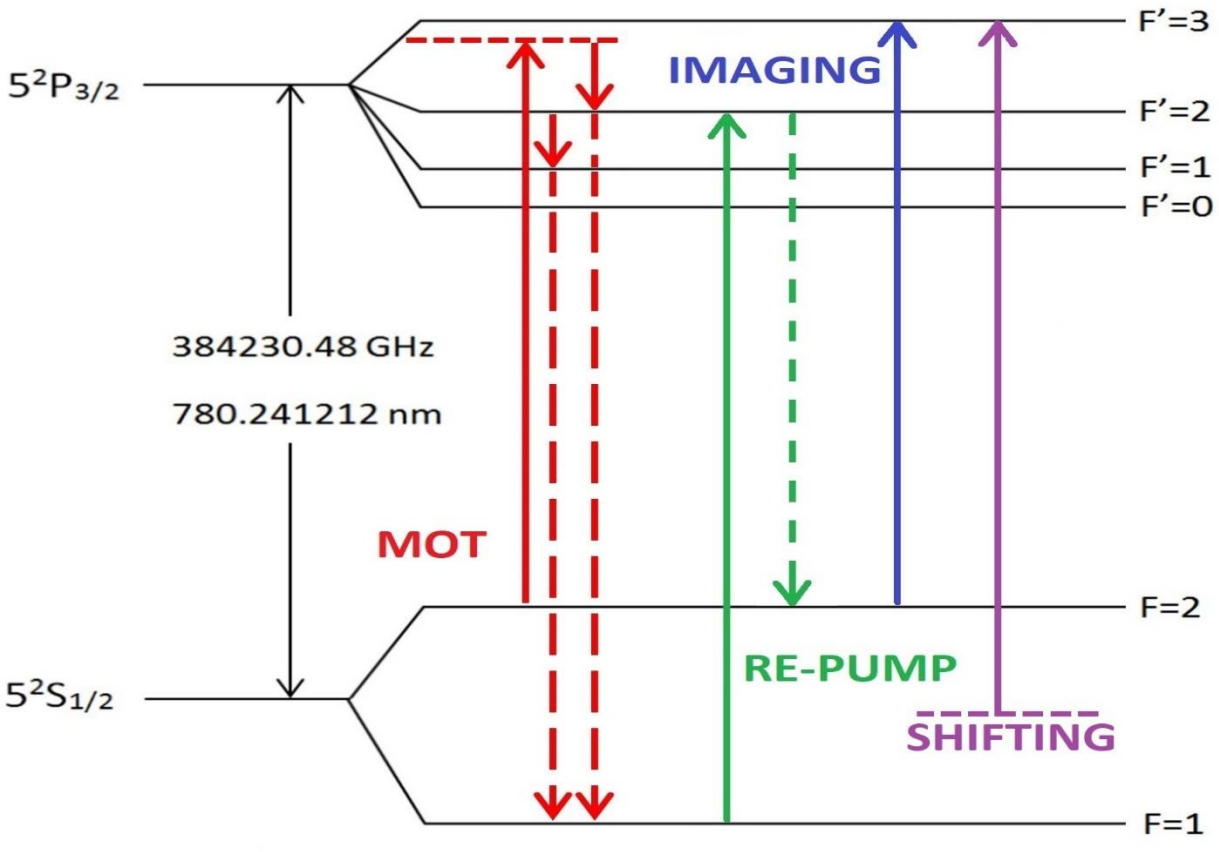

Figure 5.3: The various optical transitions for the Main, Re-pump, and shifting lasers. Note that only two of the detuning's for the main laser are shown. Those being the MOT and Imaging transition. The visual realization of the optical molasses transition is close to the MOT transition with a detuning of 65MHz. Modified from [7]

After all four lasers are propagating together to make a single beam, they are sent through a final AOM that is driven at a constant frequency of -80MHz. Again only the negative first-order light is allowed to propagate onward. This AOM acts as an electronic shutter with speeds much faster than a mechanical shutter could ever achieve. The final detuning after this AOM, and therefore the detuning that the atoms encounter can be calculated with the following formula

$$\delta_i = f_{ML} + 2f_{1st\ AOM} - f_{2nd\ AOM} \quad 5.1$$

Where f_{ML} is the frequency the main laser is locked to and is set to 133.3MHz, $f_{2nd\ AOM}$ is the frequency of the second AOM mentioned above, and $f_{1st\ AOM}$ is the three detuning frequencies that the first AOM will cycle through. It is clear that the three values needed for $f_{1st\ AOM}$ to achieve the three detuning's mentioned above are 99.15, 66.65, and 106.65. After leaving the second AOM, the beam is split into two different beams and sent through two polarization-maintaining single-mode fibers to another laser table that is home to the vacuum chamber and other equipment necessary for the experiment. [6,7,16]

5.2 The Re-pump Laser

In the above discussion, it was said that the main laser is set to the transition from the $5^2 S_{1/2}$, F=2 ground state to the $5^2 P_{3/2}$, F'=3 excited state. When the atoms decay from that excited state there is a chance that they will find themselves in the $5^2 S_{1/2}$, F=1 ground state and without anything in our system to remedy this state would soon be full. Therefore another laser must be set up to ensure that any atoms that decay into the $5^2 S_{1/2}$, F=1 state are immediately excited out of that state into the $5^2 P_{3/2}$, F'=2 excited state and from there the atoms can once again decay into either of the two ground states. This is illustrated in Figure 5.3. The re-pump laser was a TOPICA DL100 laser in a temperature controlled case. The same methods used by the main laser setup to examine modes and lock in on them was used for the re-pump. The same precautions were taken to prevent self-following and elliptical beam shape. The re-pump laser

was sent through a double pass AOM setup as well where only positive first-order light was allowed to continue propagating into one of the fibers where it was mixed with the main laser light before being injected into the vacuum chamber. A schematic of the re-pump laser setup is seen in Figure 5.4. [6,7,16]

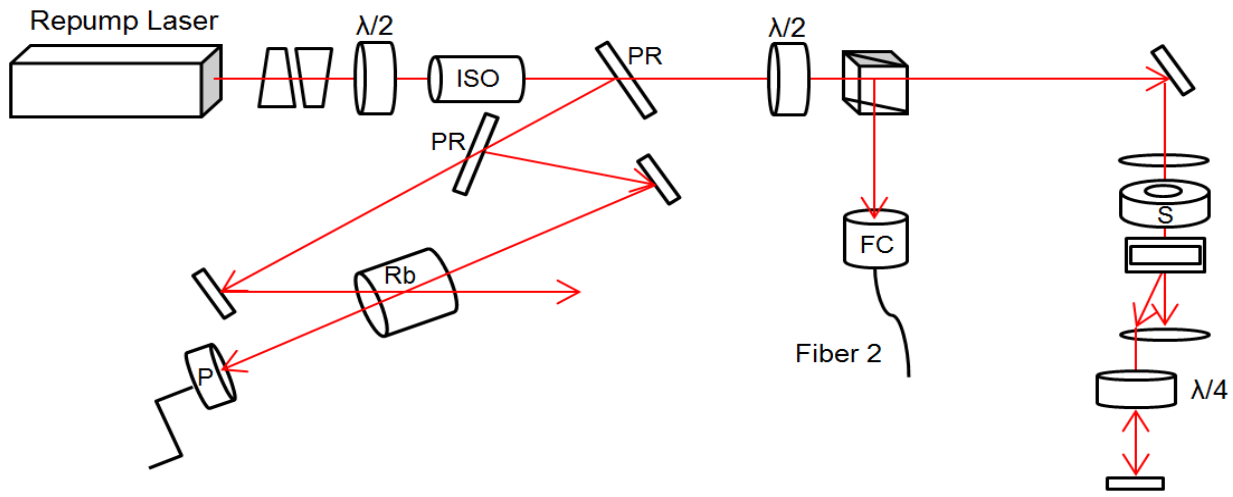

Figure 5.4 Schematic for the layout of the re-pump laser [7]

5.3 The Vacuum Chamber and Magnetic Field

The Vacuum Chamber is where all the efforts involving the Lasers and magnetic fields converge. It is made by MDC Vacuum Products and can maintain a vacuum of about 10^{-10} Torr With the help of an automatic Varian style 8 liters/second ion pump powered by TerraNova 751 controller. The Chamber boasts:

- 4 two-inch diameter quartz viewports that are specially coated with an antireflection film. These viewports are utilized by the MOT and Shifting beams.
- 4 one-inch diameter ZnSe viewports utilized by the CO_2 laser
- 2 five-inch diameter quartz viewports utilized by the MOT and Imaging beams

To facilitate the MOT creation, magnetic fields must be employed. This is done by coiling wire around the 2 five-inch viewports and passing a 16A current through them in opposite directions. This configuration with opposite currents along with a separation of the two coils equal to the radius is known as an anti-Helmholtz configuration. Each coil has a radius of approximately 4 inches and was comprised of "25 turns of copper wire with a square cross-section of external dimension .125 inches and internal dimension .016 inches" [16]. With this setup and configuration, we are able to achieve a magnetic field gradient of approximately 16 G/cm in between the coils, while maintaining that the magnitude of the magnetic field is zero at the center of the configuration. A LabVIEW program is used to control the current to the coils by applying a 0-5V analog signal to a 400 A DC current supply. In addition to the two main coils mentioned above, coils are also positioned around the smaller vertical and horizontal viewports. These coils have currents flowing in the same direction and are set up to compensate for Earth's magnetic field or any other stray fields.

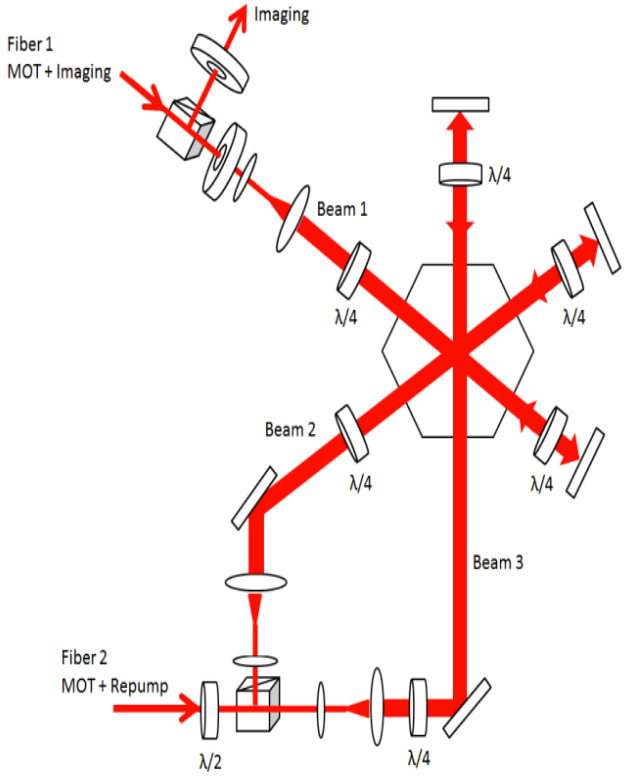

Figure 5.5: Diagram of MOT and Re-pump laser beams converging on the Vacuum chamber [7]

Once the laser exit the fiber it is split into 3 different beams and each undergoes an expansion of their spot size to approximately ½ of an inch. This is done using multiple lenses and precautions are taken to ensure the polarization is correct. The beams are directed into the vacuum chamber and retro-reflected using mirrors. The now counterpropagating beams in the ±x, ±y, ±z directions are aligned to intersect in the center of the chamber where the magnitude of the magnetic field is 0. It is

important that at various points in time during the BEC process and subsequent experiment that the re-pump or MOT lasers be shut off intermittently. Electronic shutters (UNIBLITZ, LS2T2) are utilized in conjunction with the AOM's previously mentioned to accomplish this. All are controlled with a LabVIEW program. The setup described is detailed in Figure 5.5. [6,7,16]

5.4 CO_2 Laser

To facilitate the evaporative cooling required in a FORT, a powerful 50 W laser is utilized. The laser is a coherent, GEM select – 50W CO_2 laser powered by an Agilent, 6573A DC power supply. It has a lasing wavelength of 10.6 μm, and as a result, optics made of traditional materials such as quartz or glass would incur damage if used because their absorption coefficients are too high. Coating the mirrors with Zinc Selenide (ZnSe) provides the alternative required for focusing the CO_2 laser. When we wish to redirect the CO_2 laser, mirrors coated with Gold are sufficient to the task.

Immediately after the laser light leaves the CO_2 laser housing unit, it passes through a water-cooled AOM made by IntraAction Corp (AGM 406-B1) and is driven by an IntraAction Modulator Driver (GE-4030H). A LabVIEW program sends an analog signal to control the AOM. The purpose of the AOM is to act as an electronic shutter, and to that end, only 1st order light is allowed to propagate into the vacuum chamber. All other orders of light generated by the AOM must be sent into a specialized beam dump.

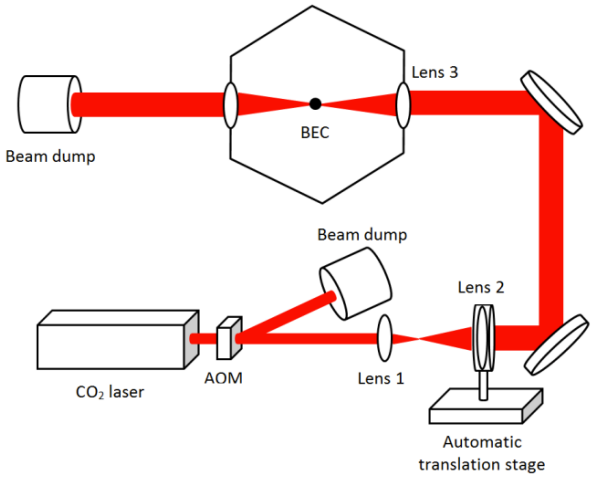

Figure 5.6: Schematic drawing for the CO_2 alignment and layout [7]

As the experiment progresses the spot size of the CO_2 laser is varied and focused. This is done using two lenses to expand the beam in a telescopic configuration, and then a third lens focuses the light upon entering the vacuum chamber. The second lens is mounted on a translation stage (Aerotech, 101SMB2- HM) that is controlled by a Soloist driver interface. After a short initial exposure, the spot size of the CO_2 laser is reduced by shortening the distance between the first and second lenses. This change in spot size is done in a few seconds. At the center of the vacuum chamber, the CO_2 laser beam has a spot size of $\omega_0 = {}^{\lambda f}/_{\pi R}$. Where R is the radius of the beam incident on the third lens, and f is the focal length of the focusing lens (~1.5in). Figure 5.6 corresponds to the CO_2 layout discussed. [6,7,16]

5.5 Microwave Setup

To generate microwave pulses at the desired frequency, a frequency mixer (Marki Microwave) was utilized. The first signal was generated using a Rb atomic clock generating a 10MHz reference signal which was passed to the locking signal for a 6.8 GHz crystal oscillator (Microwave Dynamics; PLO-4000), this resulted in a continuous 6.8GHz signal. The second signal was a pulsed RF signal that was set to ~34.682610MHz. Although the length, phase, and frequency could be altered via a LabVIEW program which then sent a signal to a programmable waveform generator (HP, HP8770A), the frequency was hardly ever adjusted. A schematic of the MW setup can be seen in Figure 5.7, and the energy transitions can be seen in Figure 5.8. [7]

Although previous experiments in this lab had synchronized the microwaves pulses and shifting laser kicks, this experiment required additional control over the microwaves lengths and phases without affecting the frequency. While this additional control was attainable, it prohibits any real synchronization of the pulses. Therefore steps to ensure that the microwaves and laser light from the shifting laser did not overlap must be taken. Mainly whenever a sequence was

prepared, it would have to be verified on an oscilloscope prior to performing the experiment and collecting data.

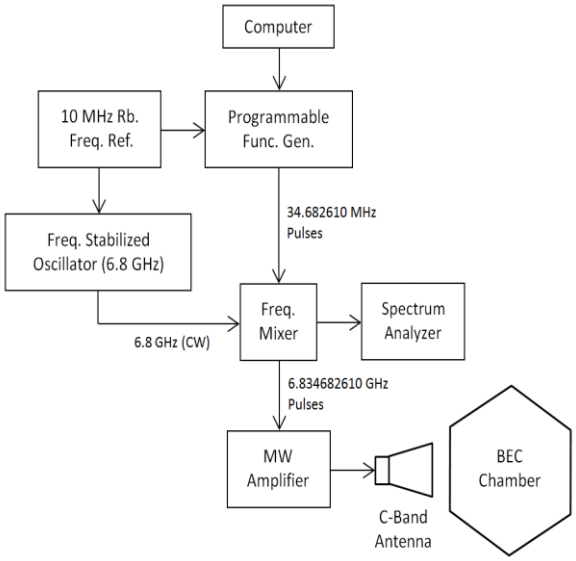

Figure 5.7: Schematic outlining the Microwave setup [7]

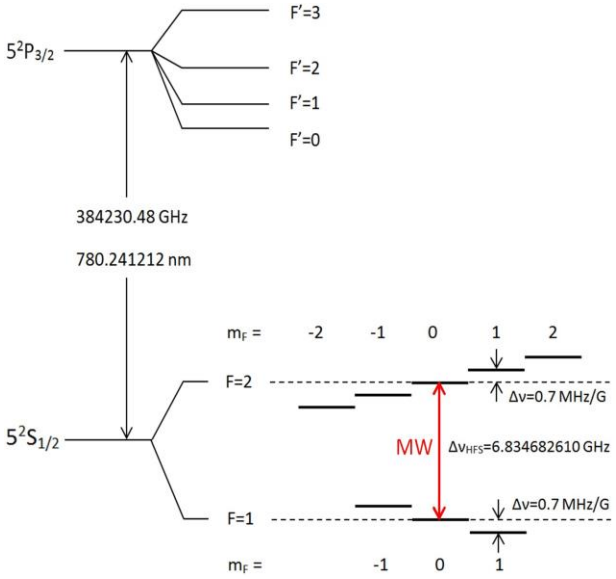

Figure 5.8: The Microwave frequency transition [7]

5.6 The Shifting Laser

The shifting laser is located on the same table as the vacuum chamber. The setup and alignment followed a similar method to the main laser, meaning that the power output was amplified using the same method of injection locking a slave laser, the mode was verified using saturation spectroscopy, and AOM's were utilized as electronic shutters. The layout can be seen in Figure 5.9. The laser used for shifting operations is a grating stabilized Toptica, DL100 laser in a temperature controlled housing.

The laser frequency was set to be approximately halfway between the $5^2 S_{1/2}$, F=1 and F=2 ground state to the $5^2 P_{3/2}$, F'=3 excited state, illustrated in Figure 5.3. This ensured that the

atoms in either ground state would experience the same perturbation when exposed to the light. Prior to the interaction of the beams with any AOM, it is split in half. Each beam then passes through its own AOM (Isomet, 40N AOMs), and first-order light is allowed to propagate into the vacuum chamber. Each beam made ~53° angle with the vertical while intersecting in the middle of the chamber. Although the beams were made to intersect and create a standing wave, this, as far as my experiments were concerned, was only utilized to verify the alignment of the shifting laser, ensuring that each beam would hit the BEC from either side. For my experiment only one beam was needed and the other was shut off by simply by setting the amplitude of the signal sent to one of the AOMs to zero. This signal is sent from a programmable waveform generator (HP, HP8770A). The signal travels from the generator into a 1-W amplifier before finally being sent to the AOM. Each AOM had its own generator, and each was controlled via a LabVIEW program [7,16]

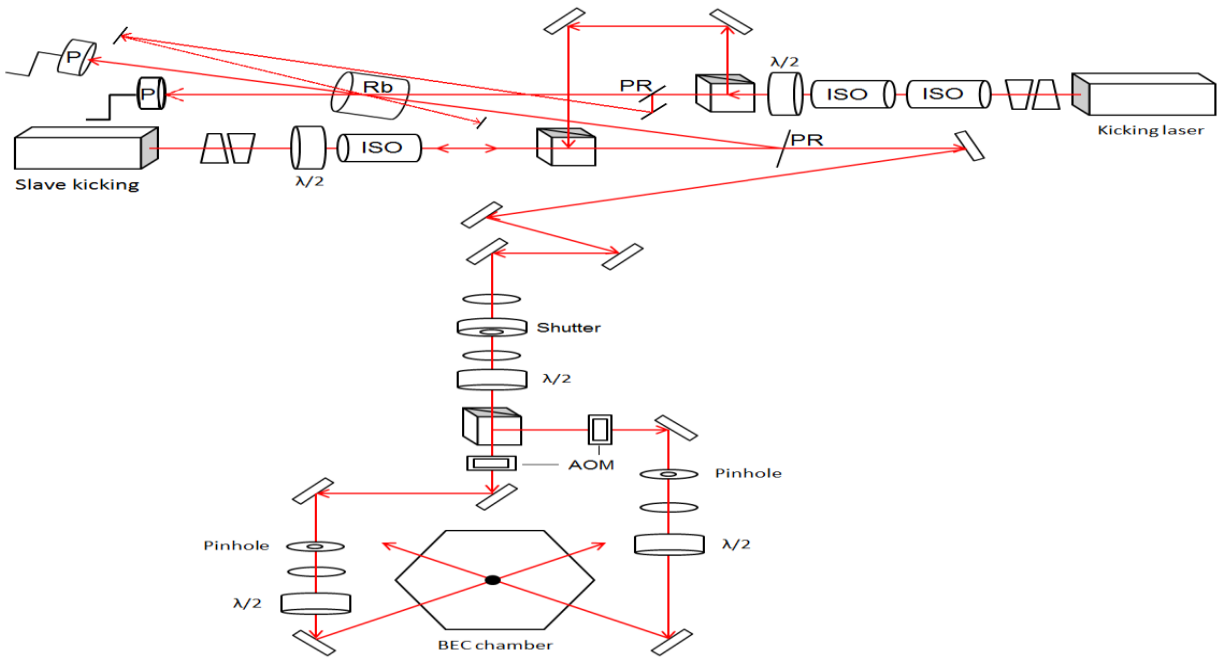

Figure 5.9: Setup for the Shifting laser. Note that by shutting off one of the AOM's only one beam will enter the BEC chamber. [7]

5.7 The Imaging Setup

An important step in any experiment is the acquisition of results, in this case, imaging the BEC. The timetable for imaging the BEC goes as follows; first, the BEC is created and held in place by the far off-resonance light of the CO_2 laser. Then BEC is exposed to perturbations via laser and microwave pulses. The Magnetic fields are subsequently shut off, and the BEC begins a free fall for ~12ms. It is at this moment that the BEC encounters the imaging beam. The imaging beam is on resonance with $5^2\ S_{1/2}$, F=2 ground state to the $5^2\ P_{3/2}$, F'=3 excited state. Because the light is on resonance, absorption followed quickly by spontaneous emission occurs, which promptly destroys the BEC. Nevertheless, the absorption profile (or shadow) can be detected and made to produce an image. The detection is done using a high-resolution CCD camera (Andor DV437-BU). Other CCD cameras are used to monitor the MOT in real-time. The camera's operation and vitals are controlled with a LabVIEW program.

A qualitative look at how we take the images starts with a change in the intensity of a laser beam propagating along a given direction, z, given by

$$\frac{dI}{dz} = -\sigma n I \tag{5.2}$$

where n is the density of atoms and $\sigma = {\hbar\omega\gamma}/{2I_s} \propto \lambda^2$ is the scattering cross-section for a beam on resonance. ω is the laser frequency, γ is the natural linewidth, and I_s is the saturation intensity. The solution to equation 5.2 is straight forward

$$I(x,y) = I_0(x,y)e^{-\sigma\tilde{n}} \tag{5.3}$$

where $\tilde{n} = nz$ is the column density or the number of atoms per unit area. If we preserve a ratio of ${I_0}/{I}$ and solve for ñ we arrive at

$$\tilde{n} = \frac{1}{\sigma} ln\left({}^{I_0}/_{I}\right) \tag{5.4}$$

In our setup, two images are taken. The first image, $I(x, y)$, is an image with the absorption profile of the atoms present. The second image, $I_0(x, y)$, is a background image taken without any meaningful amount of atoms in the path of the imaging laser. The total number of atoms in the BEC can be calculated by integrating over the column density.

$$N = \left|\frac{A}{\sigma} ln\left({}^{I_0}/_{I}\right)\right| \tag{5.5}$$

Where an absolute value has been taken to ensure a positive outcome, and the area in question is A. When dealing with the case of the CCD cameras, two things must be taken into consideration, the size and number of pixels. So if the area in question, A, is equated to the scaled area of a pixel $(\sim 13\mu m)^2$ the final calculation for the number of atoms is [6,7,16].

$$N = \left|\frac{A}{\sigma} \sum_{Pixels} ln\left({}^{I_0}/_{I}\right)\right| \tag{5.6}$$

CHAPTER VI

RESULTS AND DISCUSSION

6.1 Data Acquisition

To observe the photon echo phenomena, a precise sequence of microwaves and laser pulses must be implemented. Although our lab had a functioning program that manipulated microwaves and laser pulses to achieve quantum random walks, it was not suited to provide control over the microwaves that was needed to observe photon echo. Therefore an effort to augment the LabVIEW program was undertaken and accomplished. Because this program and subsequent augmentation can be accomplished any number of ways with various programming techniques, I do not plan to document the actual programming that resulted. It is the output of pulses, verified by an oscilloscope that is of real concern and is shown in Figure 6.1 and Figure 6.2 on the following page.

Figure 6.1 and Figure 6.2 show the various sequences that were utilized throughout the experiment. In each of the two figures, it can be seen that there are three (pink) microwave pulses. The first $\pi/2$ length pulse has a phase of 0, the second π length pulse has a phase of 180 degrees, the third had a phase that began at 15 degrees and went to 375 degrees in increments of 45 degrees. The 15-degree correction was implemented due to the behavior of the BEC when exposed to multiple $\pi/2$ length pulses. It was noticed during these diagnostics that the population of the $5^2 S_{1/2}$, F=2 was lowest when a phase shift of 10-20 degrees was implemented. The cause of this was not fully investigated, although the prime suspect is simply that we were

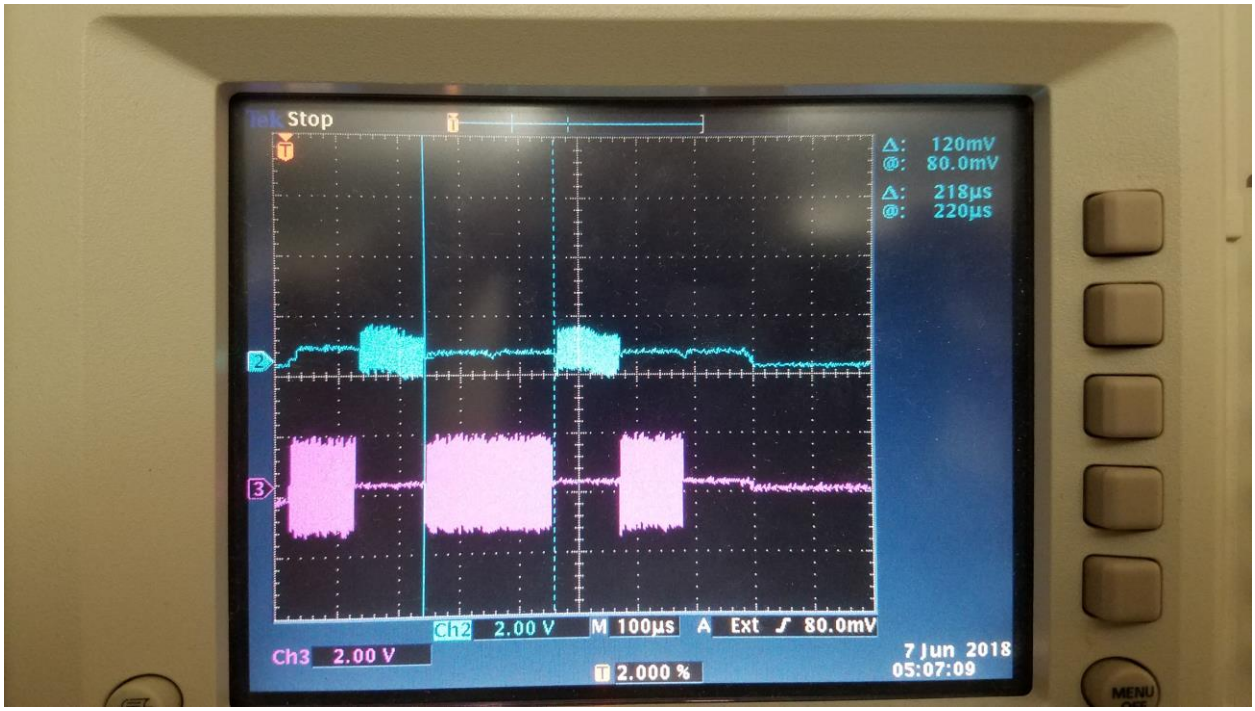

Figure 6.1: Oscilloscope output with laser light in both gaps. The blue output is the laser signal. The pink output is the microwave output.

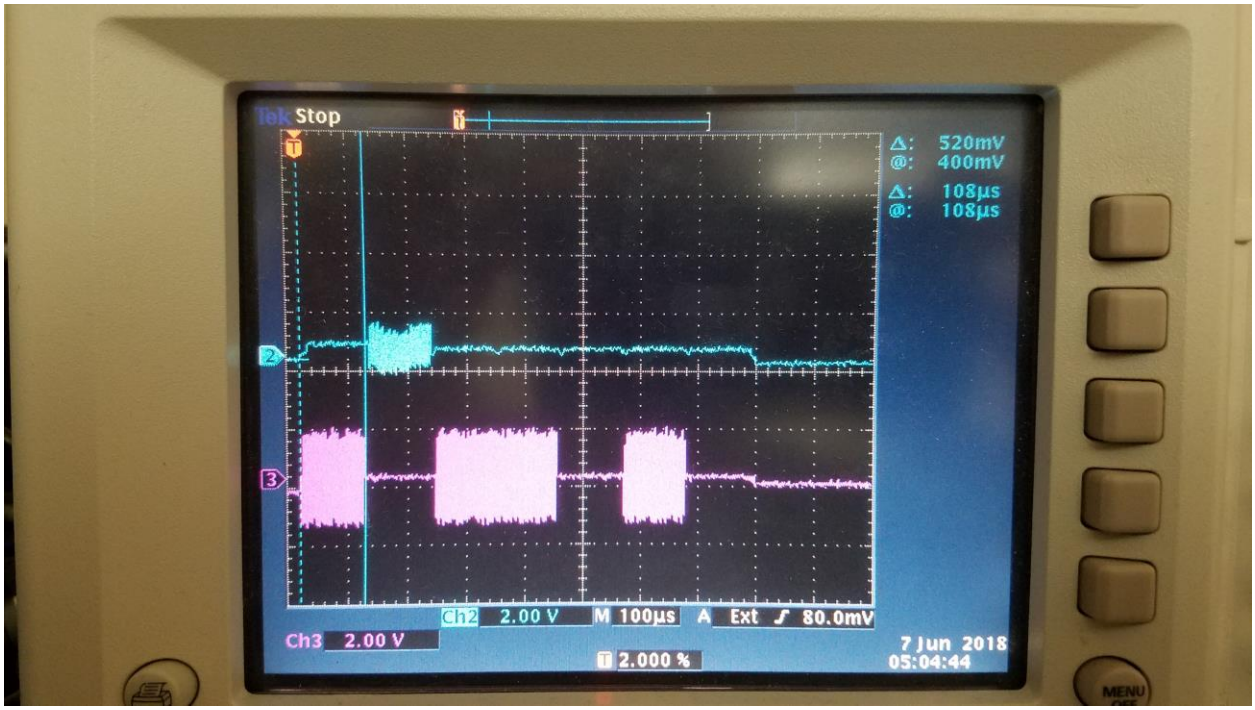

Figure 6.2: Oscilloscope output with laser light in the first gap. The blue output is the laser signal. The pink output is the microwave output.

close to the Rabi frequency with our microwave pulses but not exactly on resonance. It can also be seen in Figure 6.1 and Figure 6.2 that there are laser signals, represented in blue, that do not overlap the microwaves pulses. The laser signals were implemented to motivate a phase shift in the atoms by causing a light shift in the atoms, as was discussed in chapter 4.

Once the BEC was exposed to the microwave and laser sequence for each phase setting, from 15 degrees to 375 degrees, images were taken and an estimate for the number of atoms in that image was made. The number of atom estimate, for the eight main runs, is shown in Figure 6.3.

	Light in Both Gaps				Light in First Gap			
Degree	0.45mW	1.21mW	2.28mW	3.61mW	0.45mW	1.21mW	2.28mW	3.61mW
15	1690	2182	4848	9986	19414	68347	15725	35114
60	11452	14199	12090	14729	5250	63755	28070	41729
105	30639	32805	29589	32558	2929	47674	38389	38742
150	47200	46727	43308	48849	21464	33090	54822	26285
195	50850	59495	48789	53729	41970	8869	42240	25267
240	38382	45033	43660	47122	47277	14653	32403	16365
285	23944	30905	27854	33235	47857	17083	15859	14734
330	7315	13398	9769	17300	34372	44949	8136	28714
375	813	1293	3685	8164	18860	55119	6049	38990

Figure 6.3: Number of atom estimates for the eight phase scan runs.

Once the estimates were made, the nine images in the phase scan were combined into one image. In total, eight phase scans were completed at laser power settings of .45mW, 1.21mW, 2.28mW, and 3.61mW. The original images can all be found in Appendix A: Phase Scan Images For convenience two composite images were made of the combined images that were taken with light in both gaps and light in the first gap and are shown in Figure 6.4 and Figure 6.5. In addition to the completed data runs discussed above and in Figure 6.4 and Figure 6.5, one phase scan was performed with the shifting laser in the second gap instead of the first and with a laser power of 1.21mW. The data for that individual run is in Appendix C: Second Gap Run and the single data point has been included in the final graph of the next section for completion purposes.

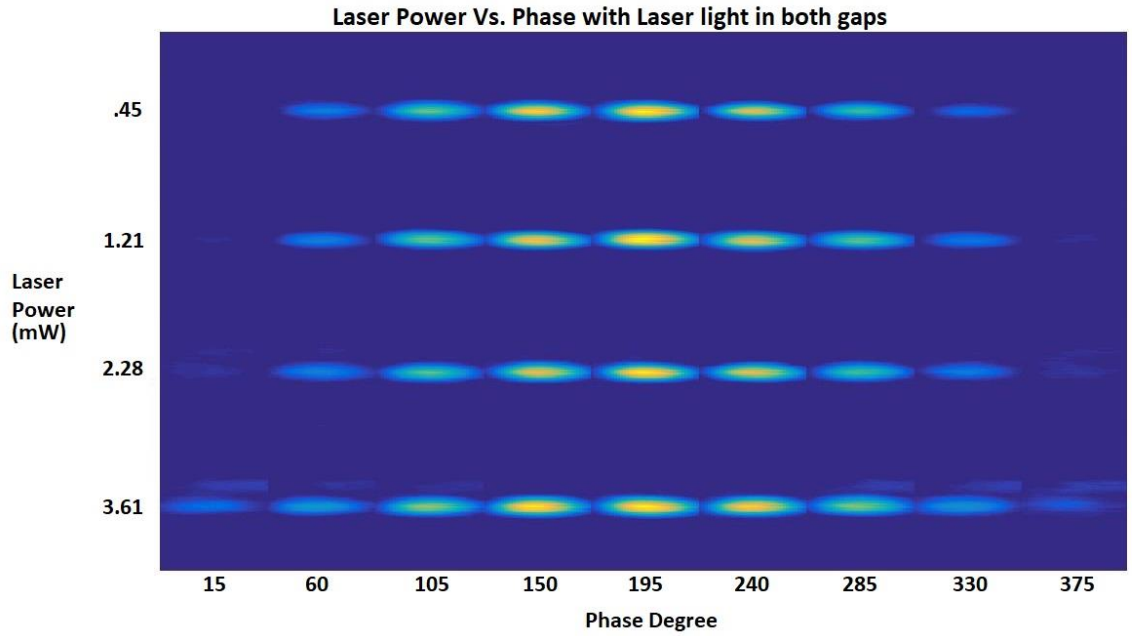

Figure 6.4: BEC Phase scan images with various laser power perturbations in both gaps

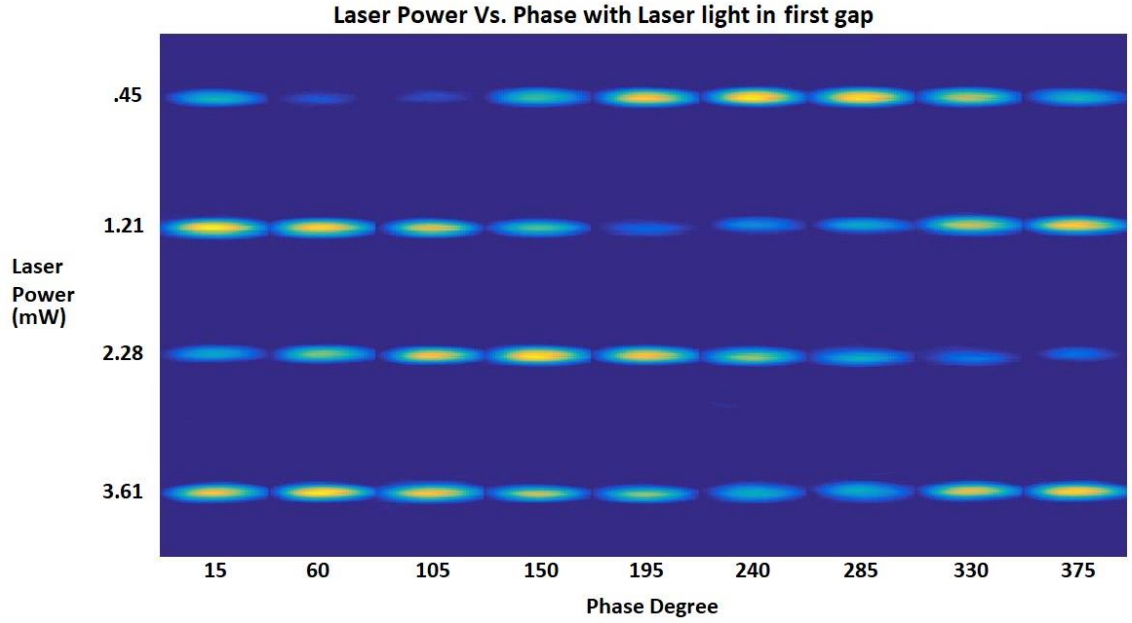

Figure 6.5: BEC Phase scan images with various laser power perturbations in the first gap

6.2 Data Processing

Upon completion of the data collection for the photon echo experiment, one should quickly realize that the atom count estimates in Figure 6.3 are not always going to contain the max/min values, due to the increments in degrees being too large. It is also clear that the atom count should be periodic in nature. Therefore it is natural to fit the data to a periodic function in order to obtain max/min values for the atom counts along with the standard error associated with those counts. The data fits were completed using a program called Sigma Plot, which utilized dynamic fitting to fit the data to the following equation.

$$N = Acos\left(\frac{2\pi\varphi}{B} + C\right) + D \tag{6.1}$$

It is clear that the argument of the cosine function was more complicated than needed and the quantity $\frac{2\pi\varphi}{B} + C$ is merely the phase that was introduced while performing the phase scan. Furthermore, it is obvious that the max/min number of atoms, N_{max} and N_{min}, is obtained by the addition/subtraction of the coefficients D and A. Sigma plot also provided uncertainties with the dynamic fitting tool, σ_A and σ_D, for the coefficients of A and D. The original data fit graphs are found in Appendix B: Best Fit Graphs and a compilation of all the fit data is in the following table.

	Light in Both Gaps				Light in First Gap			
	0.45mW	1.21mW	2.28mW	3.61mW	0.45mW	1.21mW	2.28mW	3.61mW
A	24697.81	26346.56	22746.33	22566.05	23387.03	28093.78	21520.02	12828.65
σ_A	630.62	1319.01	535.74	549.05	1359.16	2554.94	1931.82	1540.68
D	26295.85	30263.07	27369.43	32026.20	27755.71	36590.73	28750.16	28663.87
σ_D	468.70	983.00	399.26	409.23	933.30	1852.26	1383.88	1077.16
Max N	50993.66	56609.63	50115.76	54592.25	51142.74	64684.51	50270.17	41492.52
Min N	1598.04	3916.51	4623.10	9460.15	4368.68	8496.95	7230.14	15835.22
Visibility	0.94	0.87	0.83	0.70	0.84	0.77	0.75	0.45
σ_V	0.03	0.05	0.02	0.02	0.06	0.08	0.08	0.06

Figure 6.6: Fit Data and Visibility Calculation

In the above table, the concept of visibility has been applied to each of our runs in the second to last row, for our purposed visibility will be defined by the following equation

$$V = \frac{N_{max} - N_{min}}{N_{max} + N_{min}} \tag{6.2}$$

Which in terms of our coefficients, D and A, simply becomes

$$V = \frac{A}{D} \tag{6.3}$$

This simple expression allowed us to calculate and report the standard error for visibility in the last row of Figure 6.6, based off of the following expression

$$\sigma_V = \sqrt{\frac{\partial V}{\partial D}\sigma_D + \frac{\partial V}{\partial A}\sigma_A} \tag{6.4}$$

The result of this data can be represented graphically by graphing Visibility vs. Laser Power in the following figure

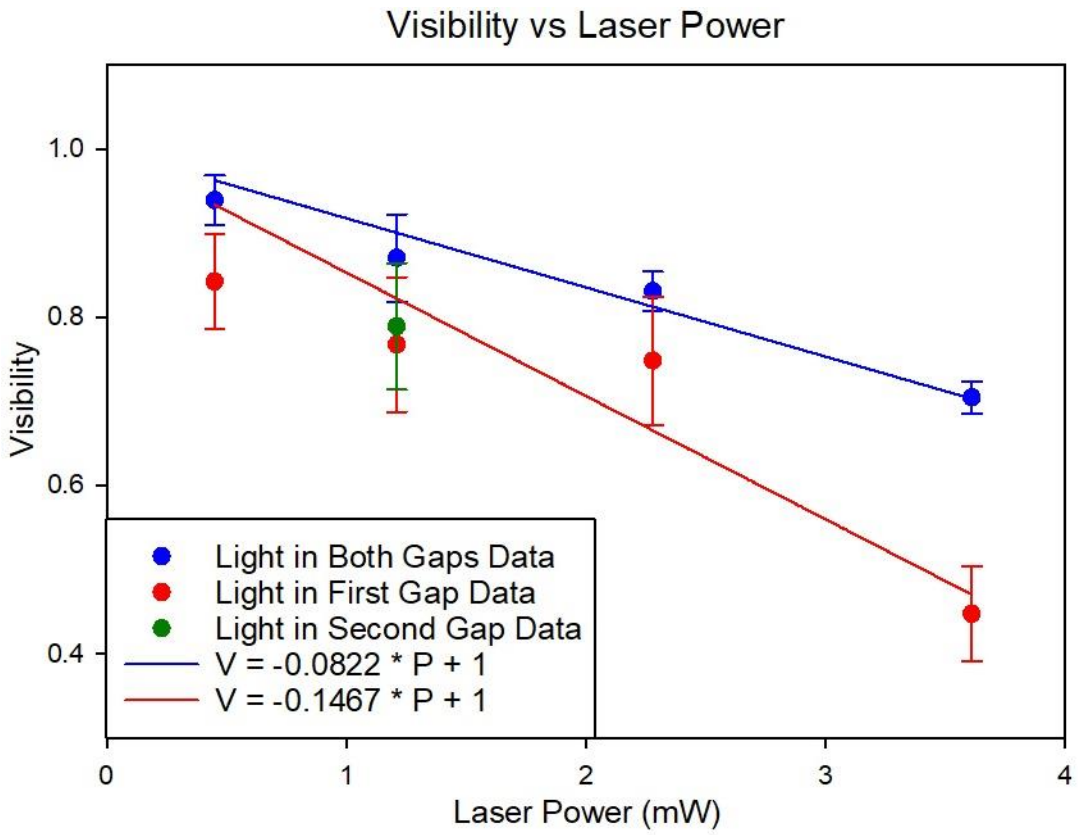

Figure 6.7: Graph of Visibility vs. Laser Power

In the graph above, the best fit lines highlight how visibility drops off as laser power is increased. It is clear that the visibility drops at a significantly faster rate when the dephasing of the dipole moments is confined primarily to the first gap. It is not surprising that the visibility would drop off even in the event of high symmetry in the pulses because there are still irreversible dephasing effects that are homogeneously affecting all atoms in the BEC stemming from incoherent interactions that are taking place. Nevertheless, the trend lines verify the presence of the photon echo phenomena by showing that equal dephasing of the dipole moments before and after a π pulse will result in higher visibility, which can be attributed to a macroscopic rephrasing of the individual dipole moments.

CHAPTER VII

CONCLUSION

The contents of this thesis were presented with a mind to provide a brief background and understanding into an experiment which aimed to realize a photon echo phenomena in a BEC. We discussed the main steps in BEC formation, the MOT and the FORT. The discussion then turned to how the on resonance microwaves and off-resonance shifting laser effect the BEC and how that effect is seen in the Bloch sphere representation as well as a working understanding of AC-Stark shift was covered. We reported on the lab equipment and how it was set up in order to experimentally realize the theories discussed. And finally, we reported on how the data for the photon echo experiment was gathered and processed. In the results, we could see that the images had much higher visibility when the dephasing laser was applied to both gaps.

There were some lab stability issues while collecting data which resulted in some less than ideal fits in the Visibility vs Laser Power Graph (Figure 6.7). Corrections to those stability issues have since been made by fine-tuning the polarization through the fibers, recalibrating the CO_2 laser's evaporation ramp, and a realignment of the re-pump laser. Unfortunately, time limitations prevented a more in-depth analysis after these stability issues were addressed. Additional data could have been obtained by running the experiment with smaller phase intervals, by performing a complete data run with the shifting laser on in the second gap instead of the first, or leaving the shifting laser off completely and investigating the phase when the length of the second gap was different than the first gap.

Investigating photon echo and how it affects our lab results is, of course, interesting in its own right. However it also provides value to future endeavors by solidifying an understanding of how our lab is able to affect the phase of the BEC states and recover dephased signals. This is useful when any quantum random walk or topology experiment requires a large number of pulses. If a large number of pulses is required, measures should be taken in order to prevent unnecessary loss of signal, which could easily be accomplished by strategically placing a π pulse and taking advantage of the photon echo phenomena.

Appendix A: Phase Scan Images

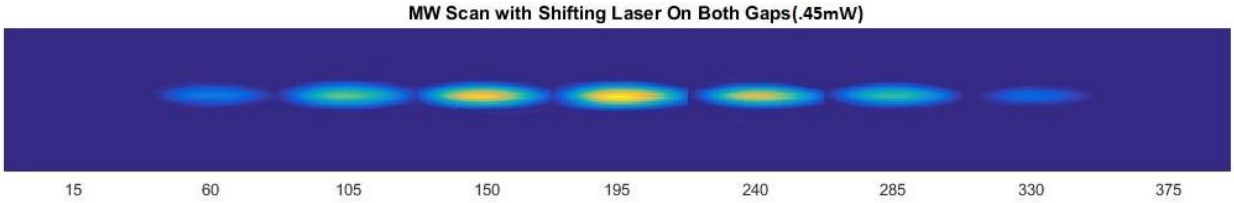

Figure 8.1: Phase scan image with a 0.45mW laser power perturbation in both gaps

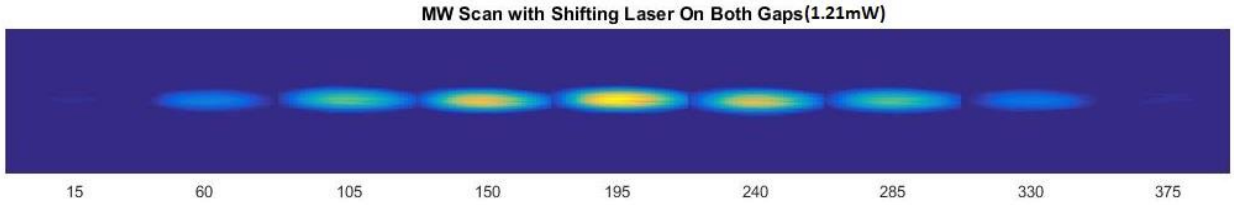

Figure 8.2: Phase scan image with a 1.21mW laser power perturbation in both gaps

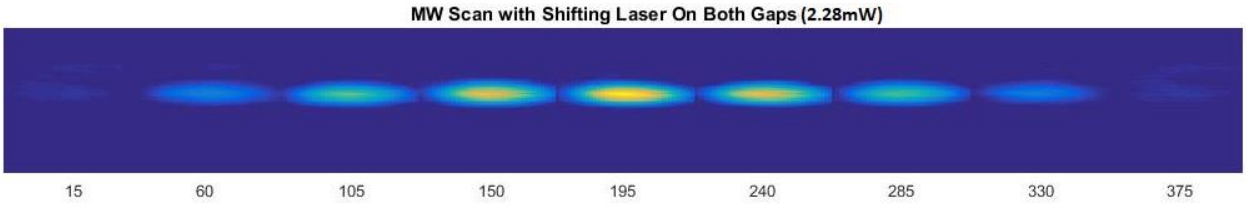

Figure 8.3: Phase scan image with a 2.28mW laser power perturbation in both gaps

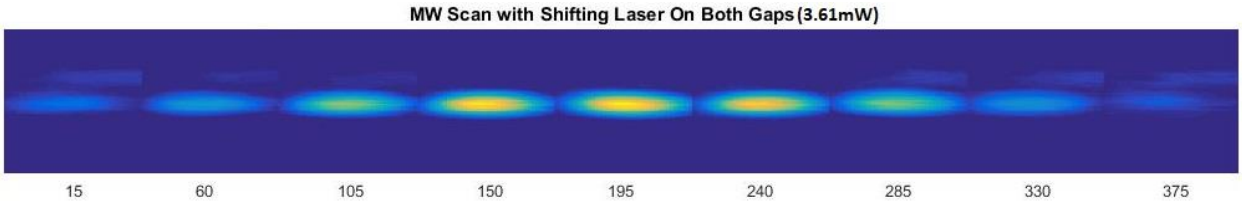

Figure 8.4: Phase scan image with a 3.61mW laser power perturbation in both gaps

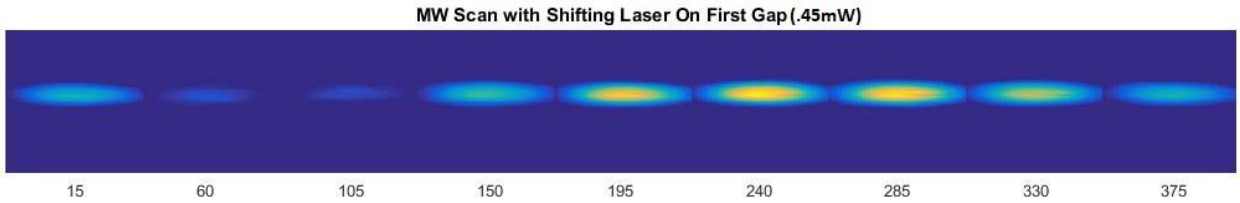

Figure 8.5: Phase scan image with a 0.45mW laser power perturbation in the first gap

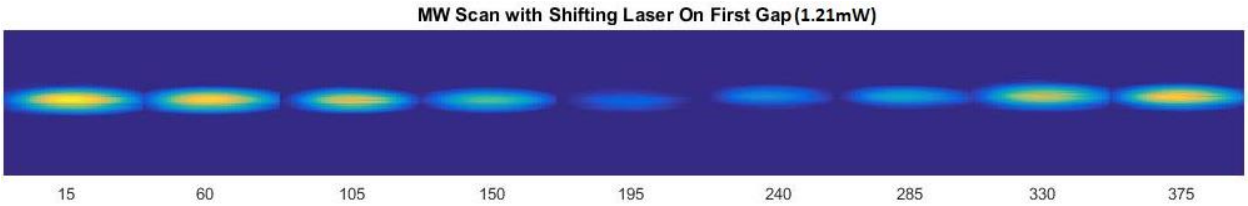

Figure 8.6: Phase scan image with a 1.21mW laser power perturbation in the first gap

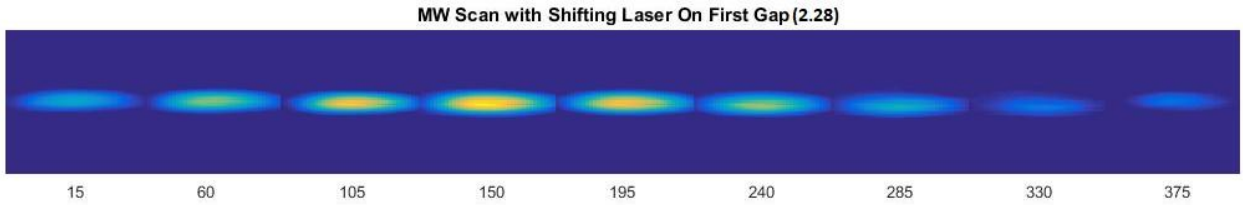

Figure 8.7: Phase scan image with a 2.28mW laser power perturbation in the first gap

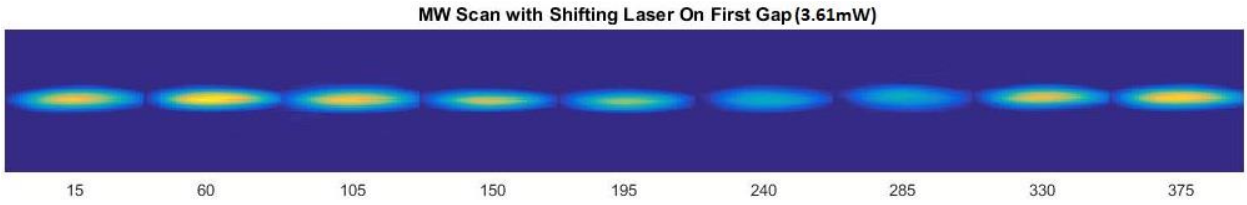

Figure 8.8: Phase scan image with a 3.61mW laser power perturbation in the first gap

Appendix B: Best Fit Graphs

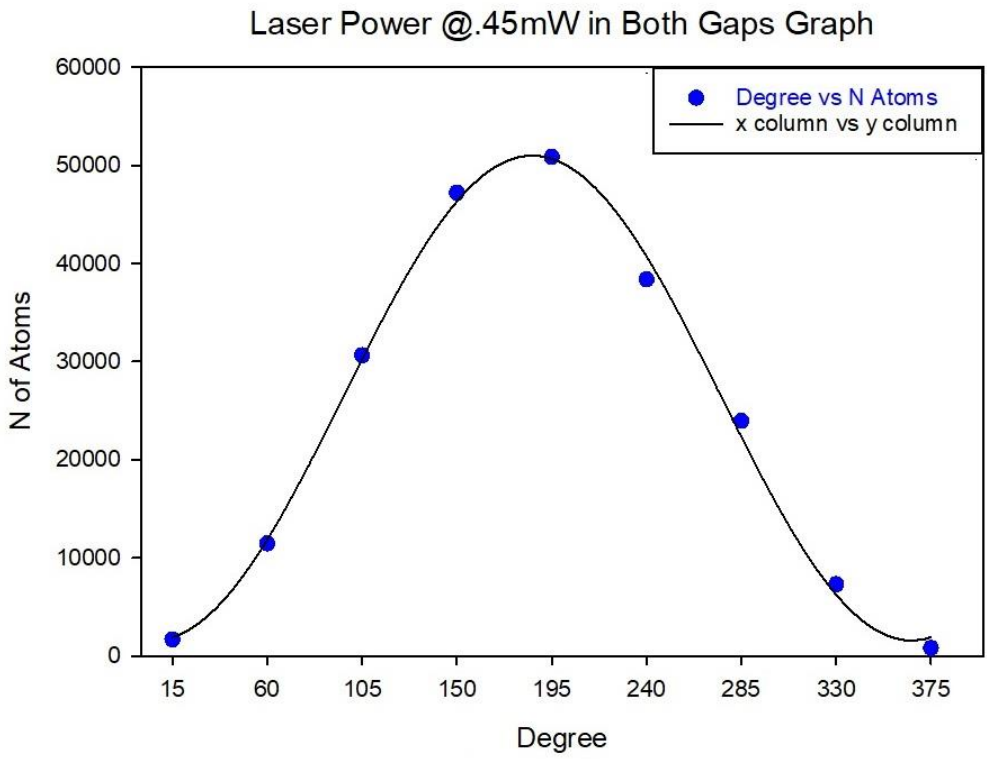

Figure 9.1: Sigma plot data fit when the laser power was at 0.45mW in both gaps

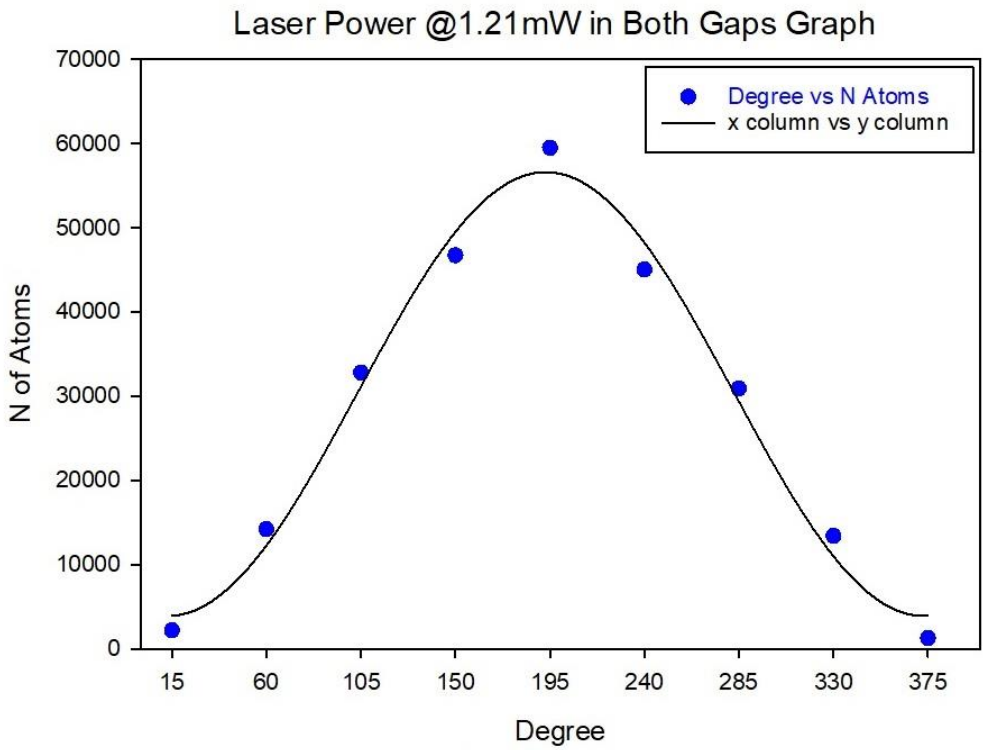

Figure 9.2: Sigma plot data fit when the laser power was at 1.21mW in both gaps

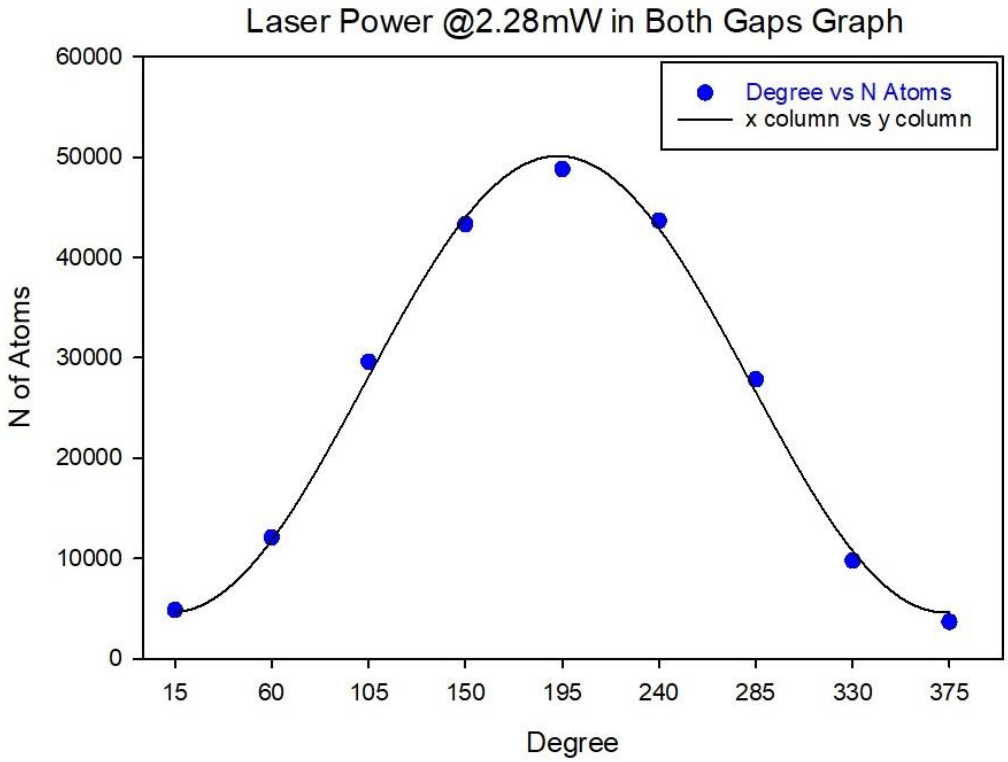

Figure 9.3: Sigma plot data fit when the laser power was at 2.28mW in both gaps

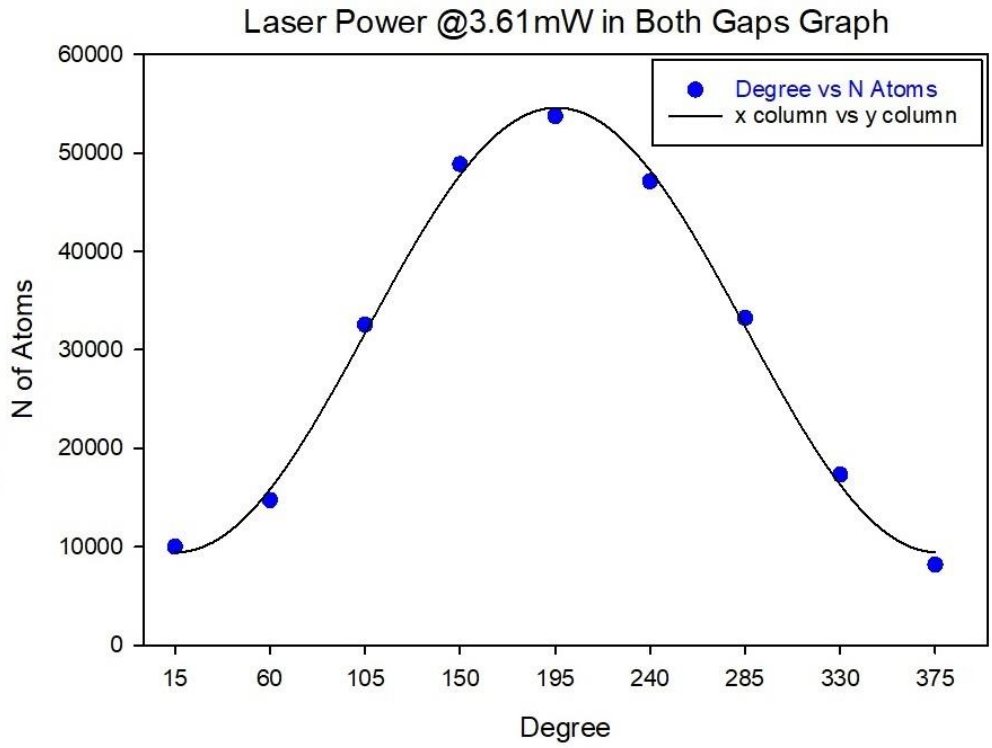

Figure 9.4: Sigma plot data fit when the laser power was at 3.61mW in both gaps

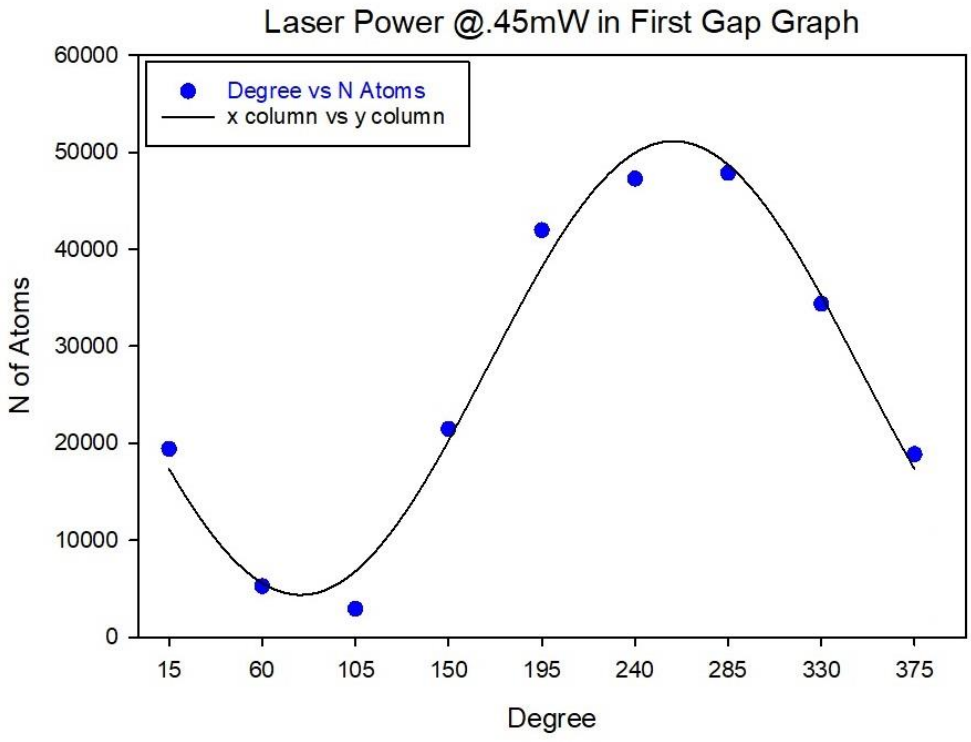

Figure 9.5: Sigma plot data fit when the laser power was at 0.45mW in the first gap

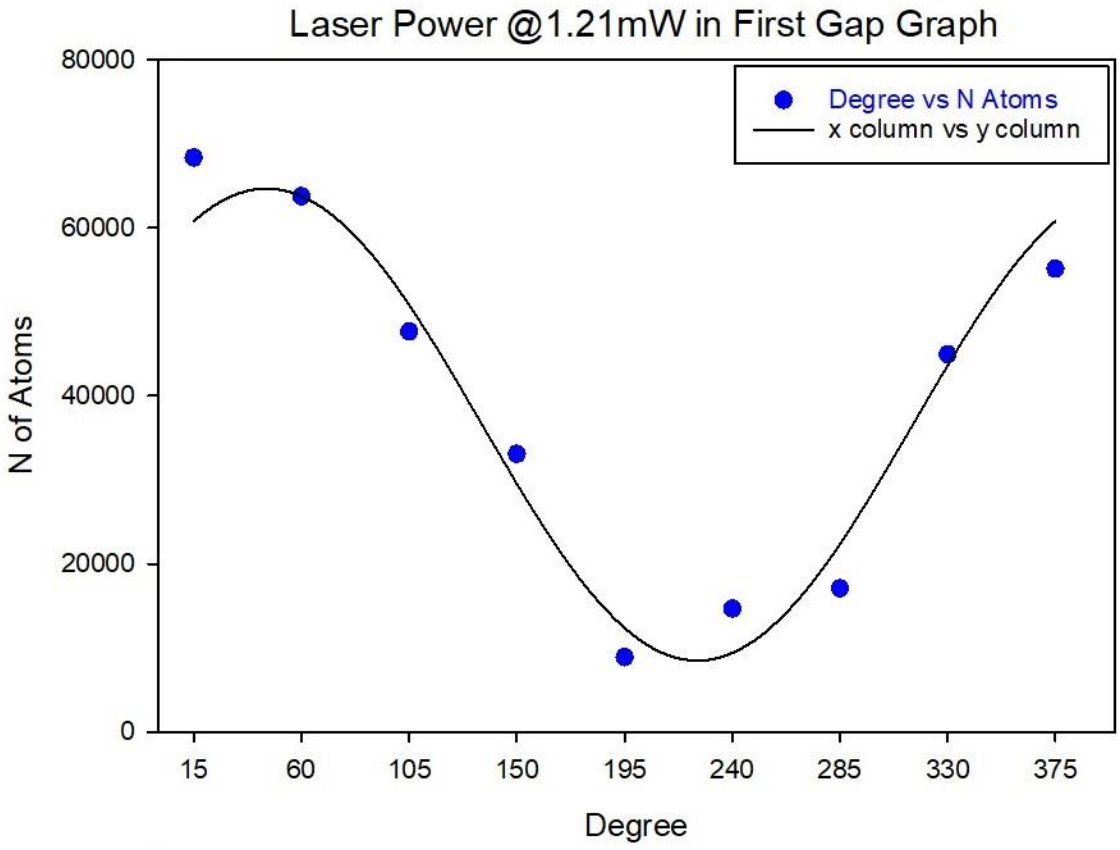

Figure 9.6: Sigma plot data fit when the laser power was at 1.21mW in the first gap

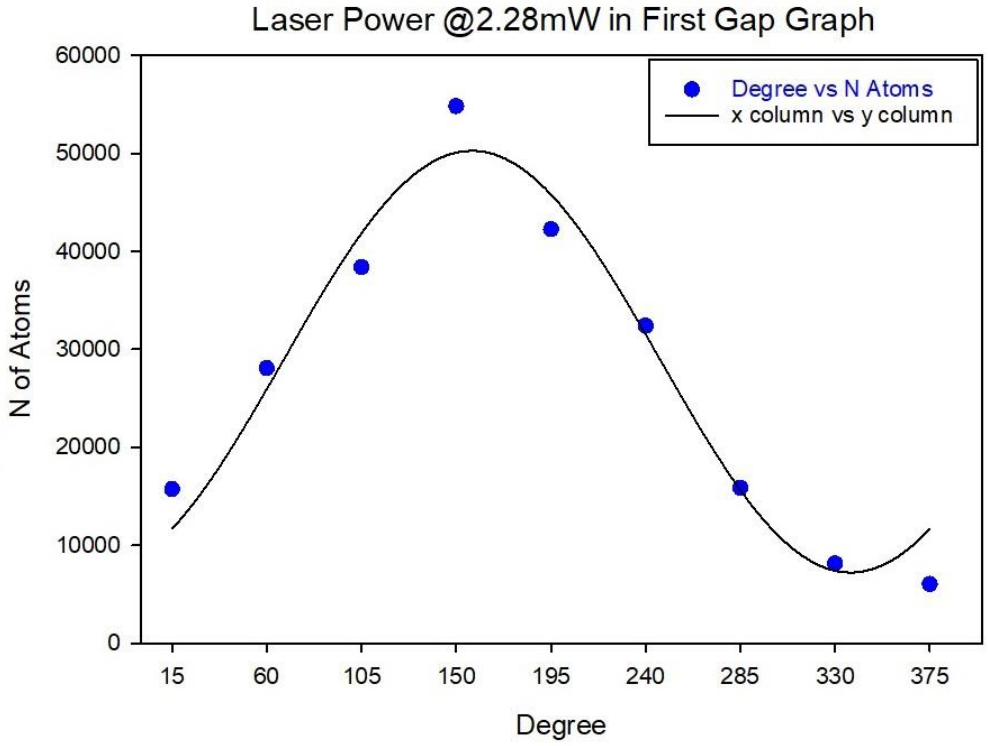

Figure 9.7: Sigma plot data fit when the laser power was at 2.28mW in the first gap

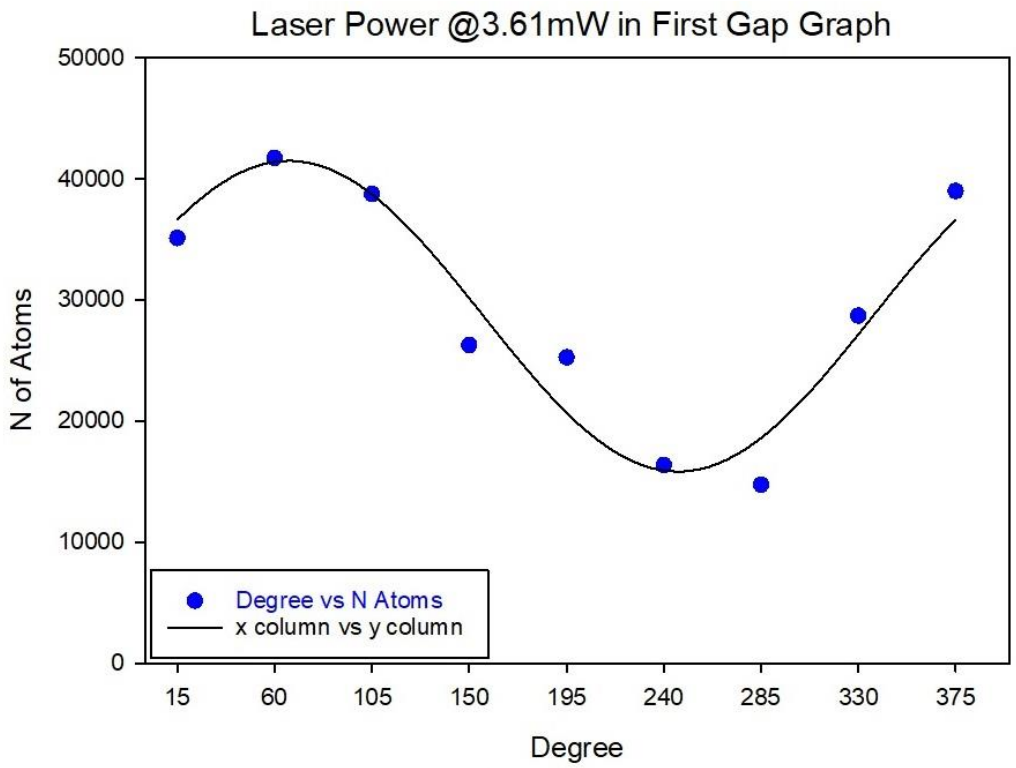

Figure 9.8: Sigma plot data fit when the laser power was at 3.61mW in the first gap

Appendix C: Second Gap Run

Light in Second Gap			
Degree	1.21mW	Sigma Plot Info	1.21mW
15	12617	A	27842.10
60	4781	σ_A	2309.70
105	21585	D	35275.25
150	48984	σ_D	1681.44
195	54449		
240	66550	Max N	63117.35
285	42552	Min N	7433.14
330	30969	Visibility	0.79
375	10357	σ_V	0.08

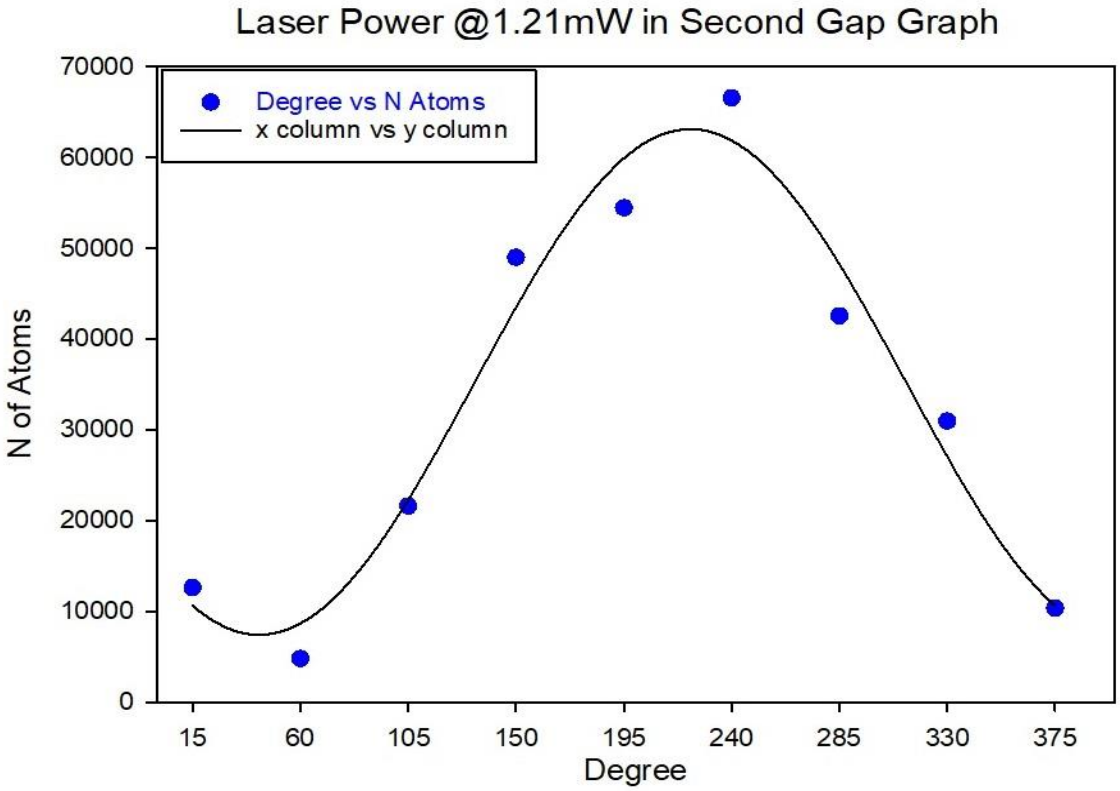

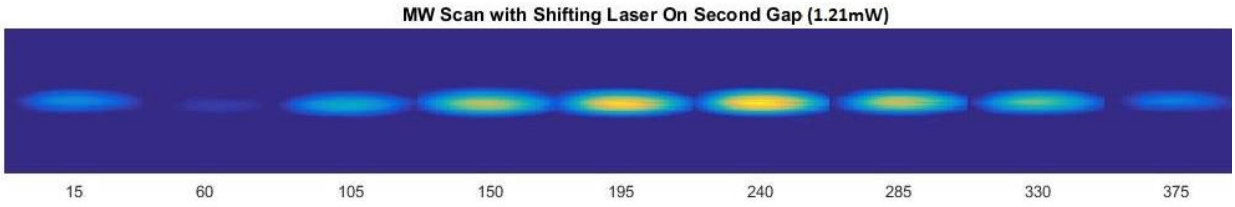
MW Scan with Shifting Laser On Second Gap (1.21mW)
15
60
105
150
195
240
285
330
375

REFERENCES

[1] W. Ketterle, Rev. Mod. Phys. **74**, 1131 (2002).

[2] L. Allen and J. H. Eberly, *Optical Resonance and Two-Level Atoms* (Wiley, New York, 1975).

[3] H. J. Metcalf and P. Van der Straten, *Laser Cooling and Trapping* (Springer, New York, 1999).

[4] W. Demtroeder, *Laser Spectroscopy 2: Experimental Techniques*, 5th edition. 2015 (Springer Berlin Heidelberg, New York, NY, 2015).

[5] J. R. Taylor, *Classical Mechanics* (University Science Books, Sausalito, Calif, 2005).

[6] R. K. Shrestha, Applications of the Atom-Optical Kicked Rotor, Ph.D., Oklahoma State University, 2013.

[7] S. Dadrasmarani, Discrete-Time Quantum Walk of a Bose-Einstein Condensate in Momentum Space, Ph.D., Oklahoma State University, 2018.

[8] R. Grimm, M. Weidemüller, and Y. B. Ovchinnikov, in *Adv. At. Mol. Opt. Phys.*, edited by B. Bederson and H. Walther (Academic Press, 2000), pp. 95–170.

[9] S. Kuhr, A Controlled Quantum System of Individual Neutral Atoms, Ph.D., 2003.

[10] A. Waxman, COHERENT MANIPULATIONS OF THE RUBIDIUM ATOM GROUND STATE, Masters, n.d.

[11] R. P. Feynman, F. L. Vernon, and R. W. Hellwarth, J. Appl. Phys. **28**, 49 (1957).

[12] D. Adam Steck, *Rubidium 87 D Line Data* (2003).

[13] O. Benson, *Quantenoptik [P23.4.1] — Nanooptik* (Humboldt-University in Berlin, 2019).

[14] J. Yepez, *Lecture Notes: Qubit Representations and Rotations* (University of Hawai'i at Manoa, 2013).

[15] C. Cohen-Tannoudji, B. Diu, and F. Laloë, *Quantum Mechanics. Vol. 2:* ... (Wiley [u.a.], New York, NY, 2005).

[16] A. Sundararaj, Atom Interferometry in a Bose-Einstein Condensate Ratchet - ProQuest, Master, Oklahoma State University, 2018.

VITA

David Judson Gary

Candidate for the Degree of

Master of Science

Thesis: EXPLORATION OF PHOTON ECHO IN A BOSE-EINSTEIN CONDENSATE

Major Field: Physics

Biographical:

Education:

Completed the requirements for the Master of Science in Physics at Oklahoma State University, Stillwater, Oklahoma in July, 2019.

Completed the requirements for the Bachelor of Science in Physics at Old Dominion University, Norfolk, Virginia in 2015.

Experience: Graduate Teaching Assistant